Tectonics

RESEARCH ARTICLE
10.1029/2021TC007014

Tectono-Metamorphic Evolution of the Northern Dom Feliciano Belt Foreland, Santa Catarina, Brazil: Implications for Models of Subduction-Driven Orogenesis

Jack James Percival[1], Jiří Konopásek[1,2], Robert Anczkiewicz[3], Morgan Ganerød[4], Jiří Sláma[5], Roberto Sacks de Campos[6], and Maria de Fátima Bitencourt[7]

[1]Department of Geosciences, UiT–The Arctic University of Norway, Tromsø, Norway, [2]Czech Geological Survey, Prague, Czech Republic, [3]Institute of Geological Sciences, Polish Academy of Sciences, Kraków Research Centre, Kraków, Poland, [4]Geological Survey of Norway, Trondheim, Norway, [5]Institute of Geology of the Czech Academy of Sciences, Prague, Czech Republic, [6]Programa de Pós-graduação em Geologia (PPGGeologia), Universidade Federal de Santa Catarina (UFSC), Florianópolis, Brazil, [7]Programa de Pós-graduação em Geociências, Instituto de Geociências, Universidade Federal do Rio Grande do Sul, Porto Alegre, Brazil

Abstract The Dom Feliciano Belt in southern Brazil and Uruguay represents the western half of a Neoproterozoic orogenic belt located in the southern portion of the South Atlantic Neoproterozoic Orogenic System. Current interpretations are divided as to the nature of orogenesis in this belt, in part owing to lacking geochronological constraints. Metamorphosed and deformed supracrustal sequences of the Brusque Complex in the northern Dom Feliciano Belt, representing part of the orogenic foreland, record the onset and duration of crustal thickening. Structural analysis and pressure–temperature estimates indicate that the complex reached peak regional metamorphic conditions of 540–570°C and 5.5–6.7 kbar during thrusting and burial, consistent with orogenic metamorphism and early crustal thickening. Garnet–whole rock Lu–Hf and Sm–Nd isochron ages date this event to between circa 660–650 Ma. Ar–Ar dating of mica suggests thrust-controlled exhumation and partial cooling by circa 635 Ma, and that localized deformation occurred into the late Ediacaran. Our results show that the orogenic foreland reached metamorphic conditions typical for crustal thickening 20–30 million years prior to the onset of massive magmatic activity in the hinterland. Such a delay is typical of hot, internal parts of orogens, which supports interpretations that hinterland magmatism in the northern Dom Feliciano Belt represents post-collisional magmatism and not arc magmatism above a subduction zone. Instead, we suggest that orogenesis in the northern Dom Feliciano Belt was initiated by rift-basin inversion driven by far-field forces transmitted through the crust in an intracontinental rift or back-arc rift setting.

Key Points:

- Clockwise P–T evolution of the northern Dom Feliciano Belt foreland records early crustal thickening and subsequent thrust-driven exhumation
- The foreland reached peak regional metamorphic conditions ca. 660–650 Ma, ~20–30 million years before voluminous magmatism in the hinterland
- The results imply the absence of a large oceanic domain between the foreland and hinterland, pointing to a rift setting prior to convergence

Supporting Information:

Supporting Information may be found in the online version of this article.

Correspondence to:

J. J. Percival,
jack.j.percival@uit.no;
jack.j.perc@gmail.com

Citation:

Percival, J. J., Konopásek, J., Anczkiewicz, R., Ganerød, M., Sláma, J., de Campos, R. S., & Bitencourt, M. d. F. (2022). Tectono-metamorphic evolution of the northern Dom Feliciano Belt foreland, Santa Catarina, Brazil: Implications for models of subduction-driven orogenesis. *Tectonics*, *41*, e2021TC007014. https://doi.org/10.1029/2021TC007014

Received 26 JUL 2021
Accepted 13 DEC 2021

1. Introduction

Orogenic systems vary widely in terms of their geometry, duration, and scale. The classic collisional orogen can be described using models that involve the termination of a Wilson cycle, where the opening and closing of a large ocean basin between continental bodies culminates in the continental collision. Accretionary orogens, in contrast, form at continental–oceanic convergent plate boundaries in the absence of continental collision, and develop during continuous subduction by crustal thickening due to short-term coupling across the subduction plate boundary (Cawood et al., 2009). Within-plate deformation can also occur away from plate margins, triggered by the transmission of stress from active plate boundaries through the lithosphere (Aitken et al., 2013; Raimondo et al., 2014). Large-scale intracontinental orogens are comparatively less common than collisional or accretionary orogens, but examples are recognized in both ancient and modern settings (Cunningham, 2005; Faure et al., 2009; Hand & Sandiford, 1999). Although the defining characteristics of collisional, accretionary, and intracontinental orogens make them distinct, Cawood et al. (2009) proposed that they represent three interrelated endmembers between which lies a wide spectrum of orogen types. Thus, continental collision at the termination of a Wilson cycle is genetically linked to preceding accretionary orogeny. Similarly, tectonic switching during accretionary orogeny can produce large-scale crustal thickening in within-plate settings (Lister & Forster, 2009), resulting in orogens that develop as the consequence of intracratonic rift inversion, similar to what occurs within an accretionary back-arc setting but at a distance from the developing arc (Collins, 2002; Thompson et al., 2001).

The South Atlantic Neoproterozoic Orogenic System (SANOS, sensu Konopásek et al., 2020) comprises an extensive system of orogenic belts that formed during the late Neoproterozoic amalgamation of Western Gondwana

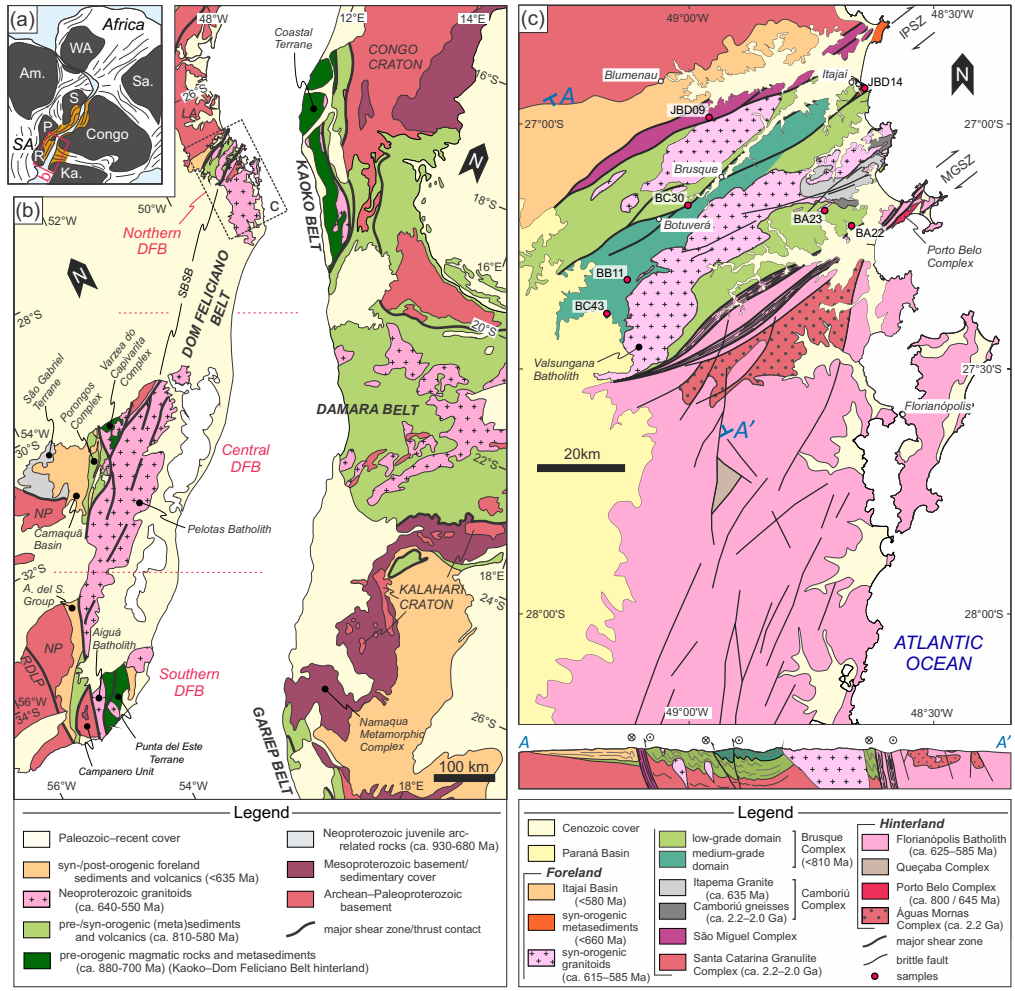

Figure 1. (a) Schematic reconstruction of the African and South American continental blocks before the opening of the South Atlantic Ocean (modified from Konopásek et al., 2020), with location of the SANOS highlighted in orange. Am. = Amazonia; WA = West Africa; Sa. = Sahara; S = São Francisco; P = Paranapanema; R = Rio de la Plata; Ka. = Kalahari. (b) Simplified geological map of the southern SANOS (based on Bitencourt & Nardi, 2000; De Toni et al., 2021; Konopásek et al., 2017; McCourt et al., 2013; Oyhantçabal, Siegesmund, & Wemmer, 2011), showing the position of the African and South American continents at the onset of the opening of the South Atlantic Ocean (after Heine et al., 2013). LA = Luis Alves Craton; NP = Nico Pérez Terrane; RDLP = Rio de la Plata Craton; SBSB = Southern Brazilian Shear Belt; DFB = Dom Feliciano Belt. (c) Simplified geology of the northern DFB (based on field mapping and collated from Basei et al., 2011; Campos et al., 2011; De Toni, Bitencourt, Nardi, et al., 2020; Florisbal, Janasi, Bitencourt, & Heaman, 2012; Hueck, Basei, et al., 2018). IPSZ = Itajaí–Perimbó Shear Zone; MGSZ = Major Gercino Shear Zone.

(Figure 1a). The SANOS is situated along the Atlantic coastlines of South America and Africa, and includes the Dom Feliciano, Ribeira and Araçuaí belts on the South American side, and the Gariep, Kaoko, and West Congo belts on the African side of the orogen. Porada (1979, 1989) first interpreted this orogenic system as having formed by collisional orogenesis after the closure of a hypothetical proto-South Atlantic Ocean. This hypothesis was later expanded upon by Hartnady et al. (1985), who proposed that orogenesis was preceded by the closure of a large oceanic domain they titled the Adamastor Ocean.

In recent years, models involving long-lived subduction of a large Adamastor Ocean, culminating in continental collision at ca. 600 Ma, have dominated much of the research surrounding formation of the SANOS (Basei et al., 2000, 2018; Heilbron et al., 2020; Heilbron & Machado, 2003). The primary evidence used to support this argument is a linear series of granitic batholiths intruding the western hinterland of the orogenic system, which are interpreted as the exhumed roots of magmatic arcs (Basei et al., 2000, 2018; Caxito et al., 2021; Heilbron & Machado, 2003; Pedrosa-Soares et al., 2001; Tedeschi et al., 2016). These include the Granite Belt in the Dom

Feliciano Belt (sensu Basei et al., 2000), the Rio Doce arc in the Araçuaí Belt (Tedeschi et al., 2016), and various magmatic complexes in the Ribeira Belt (Heilbron et al., 2020). However, in the northern SANOS, some researchers have recently moved away from standard subduction-collision models entirely, arguing that an absence of sufficient space between continental blocks precludes the formation of a large oceanic domain and long-lived subduction between the South American and African cratonic blocks (Cavalcante et al., 2018, 2019; Fossen et al., 2017, 2020; Konopásek et al., 2017, 2020; Meira et al., 2019). The existence of a large-scale Adamastor Ocean has been similarly challenged in the Dom Feliciano Belt of the southern SANOS, where evidence of the post-collisional nature of the Granite Belt (e.g., Bitencourt & Nardi, 2000; Florisbal, Janasi, Bitencourt, & Heaman, 2012; Oyhantçabal et al., 2007), and of collisional metamorphism pre-dating intrusion of the Granite Belt (Battisti et al., 2018; Koester et al., 2016; Oyhantçabal et al., 2009), casts doubt on its origins within a supra-subduction zone magmatic arc. Owing to this, some authors have proposed that the Kaoko–Dom Feliciano–Gariep orogenic system formed from the inversion of a back-arc to intracontinental rift basin where subduction occurred much earlier and further to the west (De Toni, Bitencourt, Nardi, et al., 2020; Konopásek et al., 2018, 2020; Oriolo, Oyhantçabal, Basei, et al., 2016; Oriolo, Oyhantçabal, Wemmer, Basei, et al., 2016).

Despite a generally good understanding of the Dom Feliciano Belt hinterland, owing in part to a large dataset from the Granite Belt, there are currently insufficient geochronological and P–T constraints in the foreland to develop a complete orogenic model. To investigate the above-described controversy, we have undertaken a multi-disciplinary study focusing on the pressure–temperature–time–deformation (P–T–t–D) paths of supracrustal rocks of the northern Dom Feliciano Belt foreland. By dating the growth of P–T-sensitive metamorphic minerals, in particular garnet, it is possible to constrain the timing and conditions of specific tectonic processes (Anczkiewicz et al., 2014; Baxter & Scherer, 2013), enabling reliable estimates of the timing and duration of crustal thickening during orogenesis (Godet et al., 2021; Leech et al., 2005; Smit et al., 2014). Thus, detailed structural and petrographic observations, thermodynamic modeling, Lu–Hf and Sm–Nd isotopic dating of garnet, U–Pb dating of monazite, and Ar–Ar dating of micas were utilized to constrain the conditions and timing of major tectonic events. Our results are compared with previous studies, and integrated to discuss the tectonic evolution of the southern SANOS.

2. Geological Setting

2.1. The Dom Feliciano Belt

The Dom Feliciano Belt represents the western half of the southern SANOS extending along the coastlines of southern Brazil and Uruguay (Figure 1b). The Dom Feliciano Belt is the counterpart to the Kaoko Belt and the Gariep Belt in southern Africa (Figure 1b), with the three belts sharing a common pre- and syn-orogenic evolution (Konopásek et al., 2016; Oyhantçabal, Siegesmund, Wemmer, et al., 2011; Percival, Konopásek, Eiesland, et al., 2021). The structure of the Kaoko–Dom Feliciano–Gariep orogenic system is approximately symmetric, comprising an internal *hinterland* domain characterized by high-temperature metamorphism and voluminous magmatism, bordered by western and eastern external *foreland* domains characterized by low-to medium-grade metamorphism and fold-and-thrust tectonics. The Dom Feliciano Belt is generally separated into northern, central, and southern regions located in the Brazilian states of Santa Catarina and Rio Grande do Sul, and in Uruguay, respectively (Figure 1b).

The hinterland is the easternmost domain of the Dom Feliciano Belt, and comprises granulites, paragneisses, and orthogneisses of various high-grade metamorphic complexes including the Cerro Olivo, Várzea do Capivarita, and Porto Belo complexes (De Toni, Bitencourt, Nardi, et al., 2020; Gross et al., 2009; Oyhantçabal et al., 2009). Pre-orogenic magmatism and basin sedimentation in these units occurred between ca. 810–770 Ma (De Toni, Bitencourt, Nardi, et al., 2020; Lenz et al., 2011; Martil et al., 2017; Oyhantçabal et al., 2009; Will et al., 2019). Low-pressure granulite-facies metamorphism between ca. 650–630 is interpreted as recording either the start of crustal thickening (De Toni, Bitencourt, Konopásek, et al., 2020; De Toni, Bitencourt, Nardi, et al., 2020; Konopásek et al., 2020; Lenz et al., 2011) or the inversion of plate motions leading to subduction initiation and thickening at an active plate margin (Basei et al., 2018; Frimmel et al., 2011). Voluminous granitoid magma—the Granite Belt (Figure 1b)—intruded the hinterland metamorphic complexes predominantly between ca. 630–580 Ma (Florisbal, Janasi, Bitencourt, & Heaman, 2012; Lara et al., 2020; Philipp & Machado, 2005). Some authors interpret the Granite Belt as resulting from pre-collisional arc-related magmatism above a subduction zone,

with eastward subduction culminating in the collision between the foreland and hinterland at ca. 615–600 Ma (Basei et al., 2018, 2021; Hueck et al., 2019). Other authors instead argue that the Granite Belt represents syn-to post-collisional magmatism related in time and space to syn-orogenic NE-trending strike-slip shear zones (e.g., the Major Gercino Shear Zone; Bitencourt & Nardi, 1993, 2000; Florisbal et al., 2009; Florisbal, Janasi, Bitencourt, & Heaman, 2012; Florisbal, Janasi, Bitencourt, Nardi, & Heaman, 2012; Oyhantçabal et al., 2007; Peternell et al., 2010; Philipp et al., 2013).

The foreland domain of the Dom Feliciano Belt comprises Archean–Paleoproterozoic crust of the Nico Pérez and Luis Alves terranes, which is overlain by a metamorphosed Mesoproterozoic and Neoproterozoic sedimentary cover (the Schist Belt) and late-Neoproterozoic synorogenic foreland basin sequences (Basei et al., 2000, 2009; Guadagnin et al., 2010; Oyhantçabal et al., 2018, 2021; Percival, Konopásek, Eiesland, et al., 2021). In addition, along the northern margin of the Nico Pérez Terrane in the central Dom Feliciano Belt lies the São Gabriel Terrane, which is comprised of a complex association of Neoproterozoic magmatic arcs (the ca. 890 to 860 Ma Passinho Arc and the ca. 770 to 680 Ma São Gabriel Arc), and metasedimentary and relict ophiolite complexes (Philipp et al., 2018). The Schist Belt consists of a narrow (~40 km wide) belt of deformed and metamorphosed volcano-sedimentary sequences, with early sedimentation constrained to ca. 810–770 Ma within a series of pre-orogenic rift basins (Percival, Konopásek, Eiesland, et al., 2021; Pertille et al., 2017; Saalmann et al., 2011). Early deformation and peak metamorphism in the Schist Belt is thought to be the result of crustal thickening during convergence (Battisti et al., 2018), typical of fold-and-thrust belts in convergent orogen. Although there are currently no reliable age constraints for the timing of this event, some authors have used the metamorphism in the hinterland at ca. 650 Ma as an indirect maximum age constraint (e.g., Chemale et al., 2011; De Toni, Bitencourt, Konopásek, et al., 2020), whereas Ar–Ar and K–Ar cooling ages between ca. 625–600 Ma (Oriolo, Oyhantçabal, Wemmer, Heidelbach, et al., 2016) and the intrusion of granites into the Schist Belt from ca. 615 Ma (Hueck et al., 2019) provide minimum age constraints. Synorogenic foreland basin deposits overlie the cratonic basement and parts of the Schist Belt (Figure 1b). These units consist of volcanosedimentary sequences deposited between ca. 570–540 Ma (Guadagnin et al., 2010; Oliveira et al., 2014), parts of which are metamorphosed and tectonically interleaved with metasedimentary rocks of the Schist Belt (Battisti et al., 2018; Höfig et al., 2018; Percival, Konopásek, Eiesland, et al., 2021).

2.2. The Northern Dom Feliciano Belt and the Brusque Complex

The hinterland and foreland domains of the northern Dom Feliciano Belt are delineated by the Major Gercino Shear Zone (Figures 1b and 1c). The hinterland, lying to the east of the shear zone, is predominantly comprised of the Florianópolis Batholith, which intruded between ca. 625–590 Ma and represents the northern extent of the Granite Belt (Basei et al., 2000; Chemale et al., 2012; Florisbal, Janasi, Bitencourt, & Heaman, 2012; Passarelli et al., 2010). Relicts of Paleoproterozoic basement and pre-orogenic Neoproterozoic magmatic rocks can be found within the Águas Mornas and Porto Belo complexes, respectively, which outcrop as xenoliths and roof pendants within the batholith (De Toni, Bitencourt, Nardi, et al., 2020; Silva et al., 2000). To the west of the Major Gercino Shear Zone lies the northern exposure of the Schist Belt, referred to as the Brusque Complex (Basei et al., 2000). Reworked basement units are exposed as windows within and at the northern margin of, the Schist Belt, known as the Camboriú and São Miguel complexes, respectively (Basei et al., 2011; Silva et al., 2000). The basement and supracrustal units are intruded by Ediacaran granitoid that are partly contemporaneous with the rocks of the Florianópolis Batholith, although differences in geochemistry and inherited zircon ages suggest that the two magmatic associations were sourced from distinct reservoirs (Florisbal, Janasi, Bitencourt, & Heaman, 2012; Hueck et al., 2019). To the west of the Schist Belt, separated by the Itajaí—Perimbó Shear Zone is the foreland basement of the Luis Alves Craton. Finally, overlying the foreland basement is the Itajaí Basin—a succession of syn-orogenic foreland volcanosedimentary rocks (Basei et al., 2000).

The Brusque Complex comprises a succession of volcanosedimentary rocks metamorphosed at greenschist to amphibolite facies conditions (Basei et al., 2000). The predominant rock types are metapelitic phyllites and schists, often showing narrow, alternating quartz-rich and mica-rich layering, and occasionally containing garnet. Metapsammitic and carbonate-rich layers and lenses are found throughout the complex and in some places dominate the lithology. The metavolcanic rocks are predominantly mafic to ultramafic in composition, occasionally associated with minor calc-silicate layers, and are interlayered within the metasedimentary rocks (Basei

et al., 2011; Campos et al., 2011; De Toni, Bitencourt, Konopásek, et al., 2020). Minor layers, lenses, and dykes of felsic volcanic to subvolcanic rocks are also found throughout the complex (Percival, Konopásek, Eiesland, et al., 2021).

The Brusque Complex protolith is characterized as a series of Tonian rift-related (Campos et al., 2011; Percival, Konopásek, Eiesland, et al., 2021), a transitional rift to passive margin (Basei et al., 2011; Philipp et al., 2004), or entirely passive margin volcanosedimentary successions (Basei et al., 2018). Early sedimentation in the Brusque Complex basin is constrained to somewhat before ca. 810 Ma (Percival, Konopásek, Eiesland, et al., 2021), and regional metamorphism is constrained to sometime before ca. 615 Ma by overprinting contact metamorphism caused by the intrusion of voluminous syn-orogenic granitic rocks (Basei et al., 2011; Hueck et al., 2016). Up to four separate deformation phases have been identified within the Brusque Complex (Basei et al., 2011; Campos et al., 2012; Philipp et al., 2004). Most studies describe a pervasive transposition foliation as the dominant structure in the Brusque Complex, and NW-verging asymmetric folding of this fabric is interpreted to record early top-to-NW thrusting during oblique convergence (Basei et al., 2011; De Toni, Bitencourt, Konopásek, et al., 2020; Fischer et al., 2019; Philipp et al., 2004). This foliation is interpreted as forming during regional metamorphism associated with tectonic burial, reaching maximum upper-greenschist to lower-amphibolite facies conditions (Basei et al., 2011; Campos et al., 2011; Philipp et al., 2004). According to De Toni, Bitencourt, Konopásek, et al. (2020), early thrusting was followed by the progressive transition into strike-slip dominated tectonics, leading to the development of high-angle shear zones of the Major Gercino Shear Zone, where the majority of strain was concentrated during the later stages of convergence from ca. 625 Ma (De Toni, Bitencourt, Konopásek, et al., 2020; Hueck, Basei, et al., 2018). In the Brusque Complex, deformation during the late transpressional stage is expressed by the development of upright folds and a steep crenulation cleavage. Although there are currently no reliable age constraints for this deformation in the Brusque Complex, both the early thrusting and later strike-slip shearing are thought to have occurred during the same orogenic event (Basei et al., 2011; De Toni, Bitencourt, Konopásek, et al., 2020).

3. Results

3.1. Structural Geology

Figure 2 presents the results of structural mapping and analysis in the Brusque Complex. Structural data are presented as strike/dip using the right-hand rule for plane data, and plunge/plunge direction for line data.

Field and petrological observations confirm previous studies describing the primary structural feature of the Brusque Complex as a pervasive metamorphic foliation striking NE–SW, parallel with the orogenic trend of the belt (Figures 2a and 2b). The fabric is defined by oriented white mica and chlorite in areas of low metamorphic grade, and white mica and biotite in areas of medium metamorphic grade. The foliation often contains intrafolial rootless folds (F_1), indicative of a transposition foliation (Figure 3b). Although previous studies assign this transposed fabric as the earliest S_1 (Basei et al., 2011; Philipp et al., 2004), it is unclear whether it is truly a previous metamorphic fabric or simply relicts of sedimentary S_0. Furthermore, the transposition features are consistent with synkinematic progressive shearing during primary foliation development and thus can be characterized as an early stage of the same foliation (sensu Fossen et al., 2019). Therefore, we choose to define the fabric as a whole, including transposed relicts, as S_1.

Structural domain analysis (after Vollmer, 1990) reveals two km-scale regions that diverge from the primary NE–SW trend (Figures 2d and 2e). The rocks in Region 1 (Figure 2a) are typically only weakly affected by later folding and cleavage overprint, thus best preserving the earlier orientation of the S_1 metamorphic fabric. Here, S_1 is predominantly shallowly-dipping, with the main cluster of data showing an average orientation of 135/30W (Figure 2d). Based on this region, and similarly isolated locations elsewhere, the S_1 fabric appears to be gently-dipping. NW/SE-plunging quartz stretching lineations (L_1, Figure 2c) and associated kinematic indicators, such as asymmetric quartz sigma-clasts (Figure 3a), mica fish, rotated garnet porphyroblasts, and quartz pressure shadows (Figure 4a), indicate horizontal tangential shearing and a top-to-NW shear sense. The S_1 foliation is deformed by upright to inclined folds (F_2) and an axial plane-parallel crenulation cleavage (S_2; Figure 3b). Meso-scale F_2 folding is predominantly tight, upright, and asymmetric verging to the NW (Figure 3b). This is reflected in the complex-wide S_1 foliation trend, where folding constructed from a best fit great circle is slightly

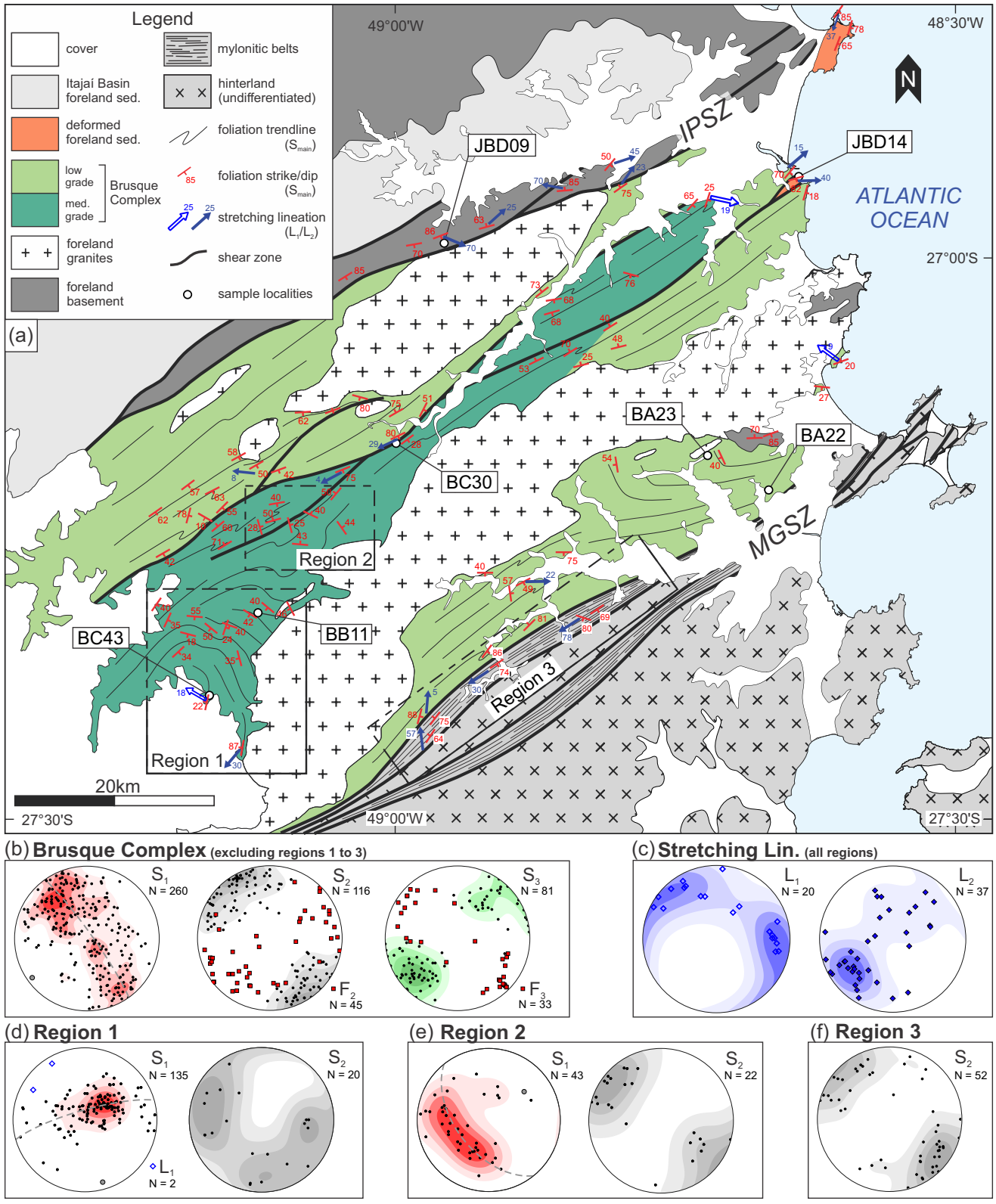
Legend
cover
Itajaí Basin foreland sed.
deformed foreland sed.
low grade
med. grade
Brusque Complex
foreland granites
foreland basement
mylonitic belts
hinterland (undifferentiated)
foliation trendline (S_main)
foliation strike/dip (S_main)
stretching lineation (L_1/L_2)
shear zone
sample localities
(a)
49°00'W
48°30'W
27°00'S
27°30'S
N
IPSZ
MGSZ
ATLANTIC OCEAN
JBD09
JBD14
BA23
BA22
BC30
BC43
BB11
Region 1
Region 2
Region 3
20km
(b) Brusque Complex (excluding regions 1 to 3)
S1 N = 260
S2 N = 116
S3 N = 81
F2 N = 45
F3 N = 33
(c) Stretching Lin. (all regions)
L1 N = 20
L2 N = 37
(d) Region 1
S1 N = 135
S2 N = 20
L1 N = 2
(e) Region 2
S1 N = 43
S2 N = 22
(f) Region 3
S2 N = 52

Figure 2.

asymmetric with an axial plane parallel to the S_2 crenulation cleavage (average orientation of 055/85E), and with a fold axis plunging shallowly to the SW (~05/235; Figure 2b). A small domain in the center of the complex (Region 2, Figure 2a), however, shows S_1 plotting along a great circle consistent with F_2 folding with an axis plunging moderately toward the NE (35/050; Figure 2e), opposite to the average trend in the majority of the complex (Figure 2b). This suggests that, on a larger scale, F_2 folding is non-cylindrical. The apparent non-cylindricity of F_2 folding is also evident in the doubly plunging nature of meso-scale F_2 fold axes (Figure 2b).

Near-complete transposition of S_1 into S_2 cleavage, predominantly defined by muscovite ±chlorite, is observed in regions of high strain (Figure 3c). S_2-parallel mylonites and phyllonites indicate even higher strain in some regions, which are most common close to the Major Gercino and Itajaí—Perimbó shear zones, although narrow phyllonitic zones are also observed in the center of the complex (Figure 2a). Where present, L_2 stretching lineations on S_2 planes in the central shear zones consist of dismembered fold limbs and other stretched quartz aggregates, and mainly plunge shallowly to the NE and SW (Figure 2c). Kinematic indicators show a predominantly dextral shear sense (Figure 4c), consistent with the major regional shear zones (Hueck, Basei, et al., 2018), although occasional symmetric and sinistral shear sense indicators are also present. The southernmost part of the Brusque Complex represents a structural domain dominated by high-strain S_2 overprint (Region 3, Figures 2a and 2f), where mylonites and phyllonites likely represent extensions of the Major Gercino Shear Zone into the Brusque Complex. Here, S_2 is predominantly steeply dipping and striking ~040°, although a subordinate cluster of data striking ~100° suggests the presence of conjugate shear zones (Figure 2f), consistent with previous observations of anastomosing mylonitic foliations within the Major Gercino Shear Zone (Passarelli et al., 2010).

The Itajaí–Perimbó Shear Zone, where the Brusque Complex is in contact with basement gneisses of the São Miguel Complex, is characterized by mylonites and strong transposition foliation. The dominant foliation (S_2) is steeply dipping and strikes ENE (Figure 2a), consistent with the orientation of S_2 elsewhere in the complex. Like in the Major Gercino Shear Zone, there are variations in the strike of S_2 consistent with a network of interconnected anastomosing high-strain zones typical of a mature shear zone (Fossen & Cavalcante, 2017). Shear sense indicators suggest predominantly dextral strike-slip movement, although moderately to steeply plunging stretching lineations at some outcrops reveal a strong top-to-WNW thrust component (Figure 4d).

A NW–SE-oriented crenulation cleavage (S_3) oriented perpendicular to the average S_2 orientation is also observed across most of the Brusque Complex (Figure 2b). This cleavage is much less ubiquitous than the previously described deformation fabrics, appearing of markedly lower strain and grade. The S_3 crenulation occasionally shows a conjugate pair at the outcrop scale (Figure 3d), which is also observed regionally where poles–to–plane data show two maxima at 320/65E and 125/50W giving a ~60° interplanar angle (Figure 2b). The S_3 cleavage is occasionally associated with meso-scale folding (F_3), which together with F_2 folds can produce dome-and-basin and other complex fold interference patterns. Macro-scale F_3 fold interference may be responsible for the spread of S_1 foliation data and F_2 fold axes away from cylindricity (Figure 2b).

3.2. Relationship Between Deformation and Metamorphism

Based on field and petrographic observations, regional metamorphism in the Brusque Complex metasedimentary rocks reached maximum lower-amphibolite facies conditions. There is an apparent increase in metamorphic grade from the hinterland toward the center of the complex, from low-grade chlorite-biotite-schists south of the Valsungana Batholith to medium-grade garnet-schists to the north (Figure 1c). There is then a sudden decrease in metamorphic grade near the center of the complex, with predominantly low-grade chlorite-schists again in the NW. The medium-grade rocks are dominated by garnet-bearing metapelitic schists, and the presence of porphyroblastic garnet is used as the principal marker defining the medium-grade zone.

Figure 2. (a) Simplified geology of the Brusque Complex (see Figure 1c for references) showing primary foliation trendlines, orientation measurements, and results of structural domain analysis. (b) Equal-area, lower-hemisphere projections showing contoured poles-to-plane data for the three deformation fabrics identified in the field (S_1, S_2, and S_3), and associated fold axes (F_2 and F_3, red squares), excluding regions 1 to 3. (c) Contoured L_1 and L_2 stretching lineations (across all regions). (d) Contoured poles-to-plane data for S_1 and S_2 in Region 1. (e) Contoured poles-to-plane data for S_1 and S_2 in Region 2. (f) Contoured poles-to-plane data for S_2 in Region 3 – note the dominant group of poles striking ~040, and two subordinate clusters defining a second group of foliations striking ~100. Dotted gray lines and gray dots in S_1 stereonets show best-fit great circles and constructed fold axes, respectively. Contouring of poles-to-plane and lineation data calculated by modified Kamb method at 5 equally spaced density levels (Vollmer, 1995).

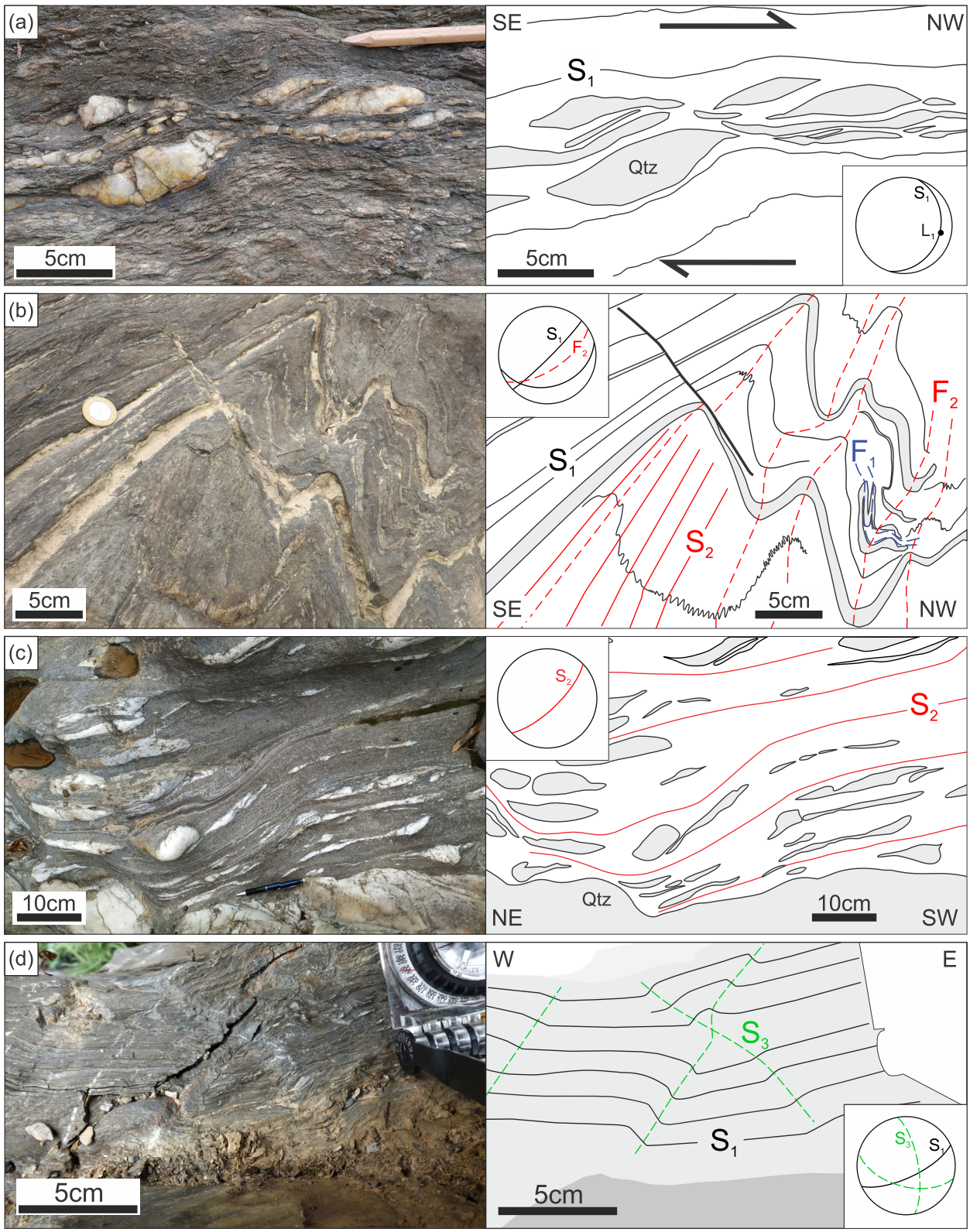
(a)
5cm
SE
NW
S1
Qtz
5cm
S1
L1
(b)
5cm
S1
F2
S1
F2
F1
S2
SE
5cm
NW
(c)
10cm
S2
S2
Qtz
NE
10cm
SW
(d)
5cm
W
E
S3
S1
5cm
S3
S1

Figure 3.

In the medium-grade domain, garnet porphyroblasts often contain oriented inclusion trails (S_i) showing continuation with the primary S_1 matrix foliation (Figures 4a & 5a–5b), and occasionally contain cores with randomly-oriented, equidimensional inclusions (Figures 5a and 5b). The overprinting S_2 crenulation cleavage is often associated with parallel chlorite overgrowth (Figure 4b), in which chlorite overprints the lepidoblastic mica-rich matrix at a high angle to the S_1 foliation (Figure 4b). Similarly, in places where there is stronger S_2 and F_2 overprint, garnet porphyroblasts often show extensive replacement by thick chlorite rims. In regions with complete transposition of S_1 by S_2, the mineral assemblage is dominated by muscovite and chlorite (Figure 4c). In the low-grade domains, the metamorphic mineral assemblage is predominantly comprised of quartz and muscovite, ±biotite, and chlorite. In the northern low-grade domain (Figure 1c), regions of apparent low strain show no indication of relict garnet or evidence of earlier higher-grade conditions. In contrast, some outcrops in the southern low-grade domain contain garnet-bearing assemblages (e.g., sample BA23) and evidence of relict garnet pseudomorphs.

3.3. Sample Petrography and Mineral Chemistry

Six metasedimentary samples and one metaigneous sample were collected from the Brusque Complex, and one deformed granite was collected from the Itajaí–Perimbó Shear Zone (Figure 1c). An overview of mineral chemistry data for samples used in thermodynamic modeling is given in Table 1, and the full dataset can be found in Data Set S1. Mineral abbreviations follow Whitney and Evans (2010). Mineral compositions and endmember mole fractions are reported as follows: X_{Mg} = Mg/(Mg + Fe), X_{Sps} = Mn/(Mn + Fe + Mg + Ca), X_{Alm} = Fe/(Mn + Fe + Mg + Ca), X_{Prp} = Mg/(Mn + Fe + Mg + Ca), X_{Grs} = Ca/(Mn + Fe + Mg + Ca), X_{An} = Ca/(Ca + Na + K).

3.3.1. Garnet-Bearing Metapelitic Samples

Samples BC43 and BB11 are medium-grained pelitic schists collected from the central medium-grade zone of the Brusque Complex (Figure 1c). Sample BC43 (S 27.39615°, W 49.16711°; all coordinates in WGS84) contains the mineral assemblage garnet (X_{Mg} = 0.05–0.10), biotite (X_{Mg} = 0.41–0.44), muscovite, plagioclase (X_{An} = 0.12), ilmenite, and quartz, with accessory chlorite (X_{Mg} = 0.47), paragonite and rutile, and trace amounts of tourmaline. The primary foliation (S_1) is segregated into layers of ~2–5 mm thickness, comprised of alternating mica + garnet-rich, and feldspar + quartz-rich domains. Garnet porphyroblasts reach up to 4 mm in diameter, often showing straight crystal faces and occasionally with thin chlorite reaction rims (Figure 5a). Garnet is an almandine-rich solid solution, with strong variation in composition from core to rim ($Sps_{0.12}Alm_{0.75}Prp_{0.04}Grs_{0.09}$ – $Sps_{0.02}Alm_{0.83}Prp_{0.09}Grs_{0.06}$). The garnet shows typical prograde U-shaped zoning of the Prp and bell-shaped zoning of the Sps components (Figure 5a), and there is a general trend of increasing Alm and decreasing Grs components from core to rim (Figures 5a and Table 1).

Sample BB11 (S 27.31695°, W 49.12598°) contains the mineral assemblage quartz, garnet (X_{Mg} = 0.04–0.09), biotite (X_{Mg} = 0.38–0.43), muscovite, chlorite (X_{Mg} = 0.41–0.45), and ilmenite, with trace amounts of plagioclase (X_{An} = 0.06–0.07), monazite and zircon. The matrix is dominated by micas, with a strong S_2 crenulation and retrograde chlorite overprint (Figure 4b). Garnet porphyroblasts are rounded, reaching up to 3 mm in diameter with inclusions of quartz and ilmenite (Figure 5b). Compositional zoning in garnet is consistent with prograde growth, with decreasing Sps and Grs and increasing Prp and Alm components from core to rim ($Sps_{0.15}Alm_{0.60}Prp_{0.03}Grs_{0.22}$ – $Sps_{0.02}Alm_{0.74}Prp_{0.08}Grs_{0.17}$; Figure 5b). Most garnet porphyroblasts show significant chlorite replacement rims (Figure 5b).

Sample BA23 (S 27.17519°, W 48.70610°) is a weakly foliated, medium-grained metapsammitic schist collected from the southern low-grade zone of the Brusque Complex (Figure 1c). The sample contains the mineral assemblage quartz, muscovite, hematite, magnetite, and garnet (X_{Mg} = 0.18–0.29), with trace amounts of biotite

Figure 3. Outcrop photographs and interpretative sketches detailing the primary deformation structures in the Brusque Complex. (a) Garnet-mica schist (S 26.94385, W 48.71592) showing the primary metamorphic foliation (S_1) and sigma-shaped stretched quartz veins indicating top-to-WNW shear sense. (b) Garnet-mica schist (S 27.19278, W 49.04884) showing intrafolial folding (F_1) within S_1 foliation, and overprinting F_2 folds and axial plane-parallel S_2 cleavage. (c) Retrograde garnet-mica schist (S 27.19229, W 49.04803) showing transposition foliation (S_2) with transposed S_1 quartz veins and F_2 fold hinges. (d) Chlorite-mica phyllite (S 27.20600, W 49.15432) deformed by low-strain F_3 conjugate crenulations (S_3 cleavage).

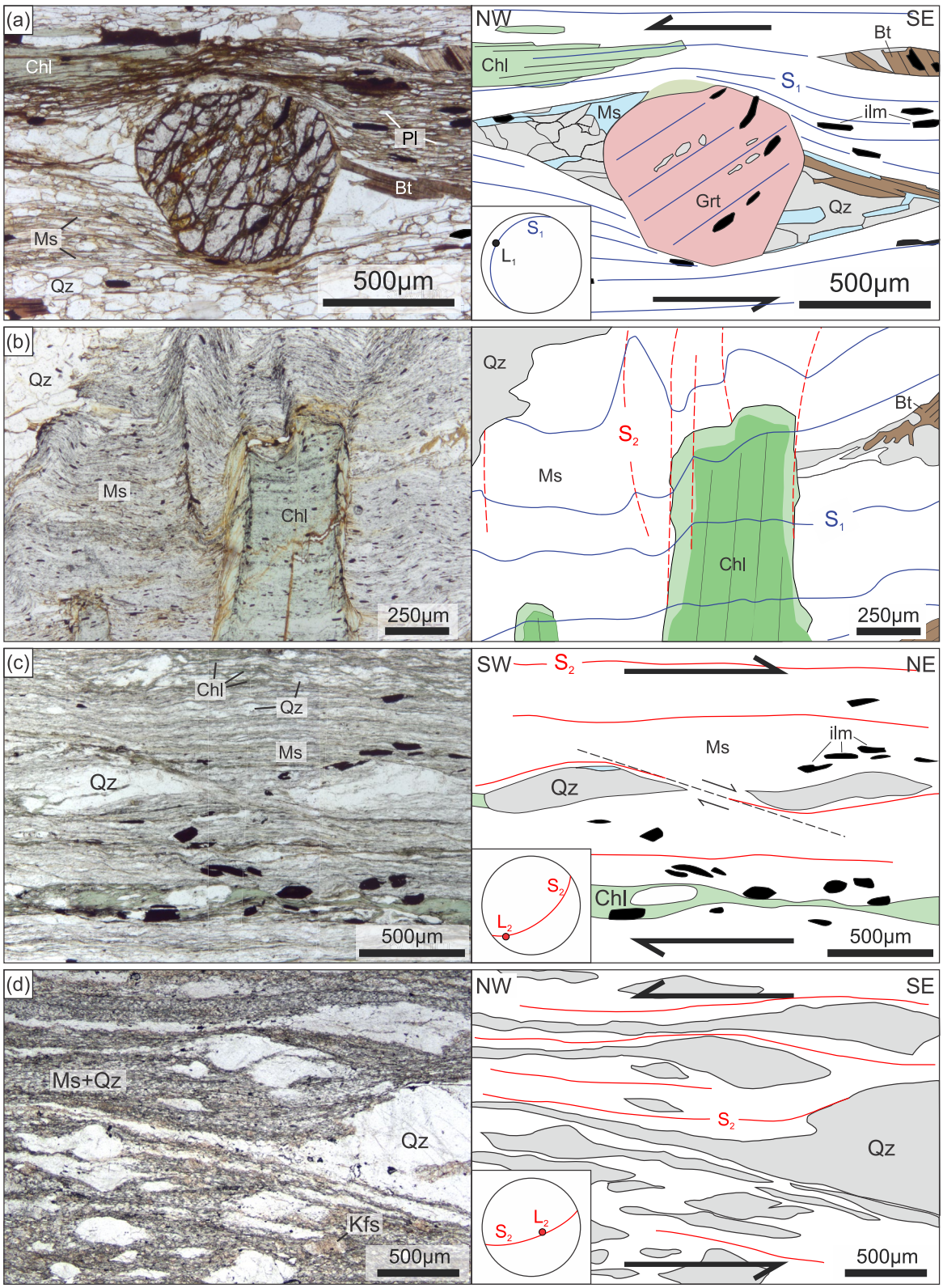
(a)
Chl
Pl
Bt
Ms
Qz
500μm
NW
SE
Chl
Bt
S1
Ms
ilm
Grt
Qz
S1
L1
500μm
(b)
Qz
Ms
Chl
250μm
Qz
Bt
S2
Ms
S1
Chl
250μm
(c)
Chl
Qz
Ms
Qz
500μm
SW
S2
NE
Ms
ilm
Qz
S2
L2
Chl
500μm
(d)
Ms+Qz
Qz
Kfs
500μm
NW
SE
S2
Qz
S2
L2
500μm

Figure 4.

(X_{Mg} = 0.74), chlorite, rutile, and tourmaline. The matrix is dominated by quartz, with abundant interstitial hematite, and occasional narrow (1 mm) lenses of muscovite and chlorite (Figure 5c). Garnet is mostly poikilitic and is found within lenses together with muscovite (Figure 5c). The mica-rich lenses show evidence of a weak S_2 crenulation, with recrystallized white mica oriented parallel to S_2. Hematite grains (<50 μm) are oriented parallel to the primary foliation and are present as inclusions within garnet porphyroblasts. Relict magnetite is found within larger hematite grains. Garnet in sample BA23 is a spessartine-rich solid solution and shows prograde core to rim compositional zoning (Figure 5c; $Sps_{0.70}Alm_{0.19}Prp_{0.04}Grs_{0.06}$ – $Sps_{0.60}Alm_{0.25}Prp_{0.10}Grs_{0.05}$).

3.3.2. Low-Grade Metapelitic Samples

Samples BC30 and JBD14 are metapelitic phyllites collected from the northern low-grade zone of the Brusque Complex (Figure 1c). Both samples contain the mineral assemblage quartz, muscovite, chlorite, plagioclase, and oxides. Sample BC30 (S 27.16005°, W 48.99434°) was collected from a steeply dipping high-strain shear zone in the center of the Brusque Complex (Figures 1c and 2a). It is fine-grained and strongly foliated, containing foliation-parallel stretched quartz veins, sigma-shaped quartz porphyroclasts, mica-fish, and S-C-C' shear fabrics indicating predominantly dextral strike-slip kinematics (Figure 4c). Neoformed quartz in shear bands cutting across quartz veins shows evidence of bulging dynamic recrystallization, indicating deformation at low-temperature conditions between ~280–400°C (Stipp et al., 2002).

Sample JBD14 (S 26.92420°, W 48.63520°) was collected on the coast, along-strike from sample BC30 in a similarly steeply dipping high-strain zone (Figure 1c). The sample is coarser-grained than sample BC30 and contains a lower proportion of matrix phyllosilicates. The microstructure involves thin phyllosilicate-rich domains anastomosing around lenses of quartz aggregates, with individual quartz grains ranging from ~50–250 μm in width.

3.3.3. Metaigneous Samples

Sample BA22 (S 27.20325°, W 48.66032°) is a fine-grained, weakly foliated metavolcanic rock collected from the low-grade domain of the Brusque Complex, close to the Major Gercino Shear Zone (Figure 1c). The sample contains the mineral assemblage quartz, albite (X_{An} = 0.00–0.10), and muscovite, with minor garnet (X_{Mg} = 0.01), biotite (X_{Mg} = 0.28–0.29) and ilmenite, and trace amounts of tourmaline. Garnet grains are small (~100 μm) and rounded, with no visible inclusions (Figure 5d). Garnet is spessartine- and almandine-rich solid solution, with no significant pyrope component (Figure 5d), and shows only minor zoning from core to rim ($Sps_{0.46}Alm_{0.50}Prp_{0.00}Grs_{0.3}$ – $Sps_{0.40}Alm_{0.56}Prp_{0.00}Grs_{0.04}$). Biotite shows poor analytical results due to alteration (see Table 1).

Sample JBD09 (S 26.9780°, W 48.9567°) is a mylonitic granite collected from the Itajaí–Perimbó Shear Zone (Figure 1c). The sample comes from the ca. 840 Ma-aged Morro do Parapente Granite (Basei et al., 2008) which intrudes the São Miguel Complex. The sample contains the mineral assemblage quartz, muscovite, plagioclase, and K-feldspar, with minor oxides. The matrix comprises ~80% of the sample, and predominantly consists of fine-grained white mica and quartz, with relict K-feldspar porphyroclasts up to 0.5 mm. Quartz porphyroclasts up to 5 mm in length show evidence of bulging and sub-grain rotation dynamic recrystallization, suggesting deformation at temperatures between ~300–450°C (Stipp et al., 2002). The foliation is steeply-dipping, and sigma-shaped quartz porphyroclasts and stretched quartz tails indicate oblique dextral strike-slip shear kinematics with a strong top-to-WNW thrust component (Figure 4d).

Figure 4. Photomicrographs and sketches detailing metamorphic textures and deformation microstructures in the Brusque Complex and adjacent units (sections with stereonets are cut along in the XZ plane, parallel to lineation and perpendicular to foliation). (a) Garnet-mica schist from the medium-grade, low-strain Brusque Complex (sample BC43) showing a rotated garnet porphyroblast with oriented mineral inclusions (S_i) and quartz-rich pressure shadows indicating top-to-NW shear sense. (b) Garnet-mica schist from the medium-grade Brusque Complex (sample BB11) showing a large retrograde chlorite porphyroblast overgrowing S_1 and elongated parallel to S_2 (note also that the F_2 crenulation is less well-developed within the chlorite suggesting growth during the early stages of S_2 development). (c) Chlorite-mica phyllite from the low-grade, high-strain Brusque Complex (sample BC30) showing sigma-shaped quartz aggregates and shear bands indicating dextral strike-slip shear sense. (d) Mylonitic part of the Morro do Parapente Granite within the Itajaí–Perimbó Shear Zone (sample JBD09) showing stretched quartz sigma-type porphyroclasts indicating mixed dextral strike-slip and top-to-NW thrusting shear sense, and showing evidence of bulging and sub-grain rotation dynamic recrystallization.

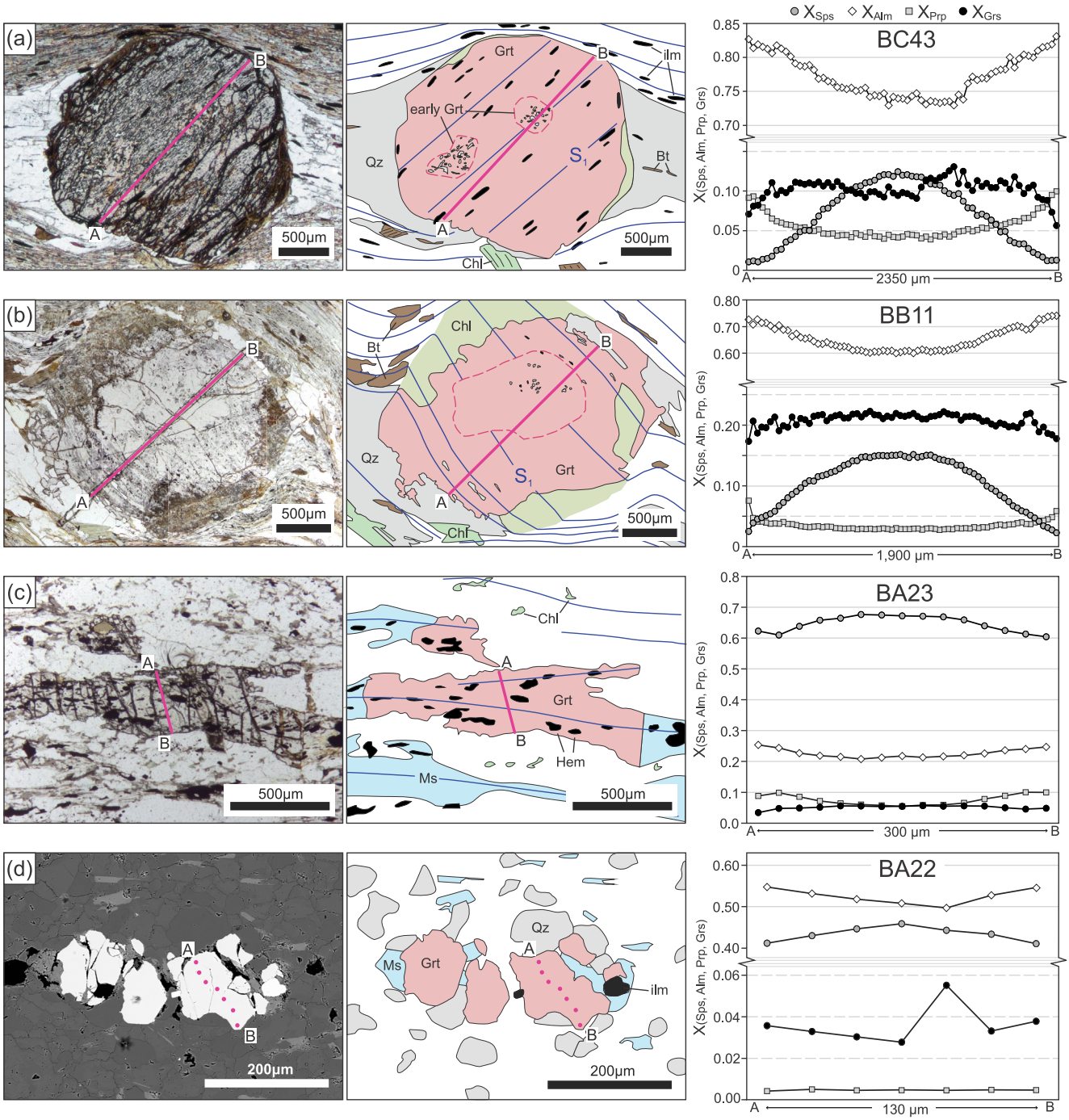

Figure 5. Garnet photomicrographs and SEM image, interpretative sketches, and compositional transects for samples (a) BC43, (b) BB11, (c) BA23, and (d) BA22. Red lines and dots on photomicrographs and sketches show approximate locations of compositional transects.

3.4. Phase Equilibria Modeling

P–T estimates for four garnet-bearing samples from the Brusque Complex were calculated using the PerpleX software package of Connolly (2005) (ver. 6.9.0) with the thermodynamic dataset DS6.22 of Holland and Powell (2011). The following solution models were used for all pseudosections: garnet, chlorite, white mica, biotite, and staurolite of White et al. (2014), and ternary feldspar of Fuhrman and Lindsley (1988). In addition, a solution model for ilmenite (White et al., 2000) was used to calculate pseudosections for samples BC43, BB11,

Tectonics

10.1029/2021TC007014

Table 1
Representative Garnet, Biotite, Muscovite, Plagioclase, and Chlorite Compositions

	BC43						BB11							BA23				BA22				
	Grt						Grt					Chl		Grt				Grt				
Sample	Core	rim	Bt	Msc	Pl	Chl	Core	rim	Bt	Msc	Pl	early	Late	Core	rim	Bt	Msc	Core	rim	Bt	Msc	Pl
wt %																						
SiO_2	36.53	36.71	36.06	46.97	66.39	25.33	37.62	37.75	36.03	46.79	68.06	25.00	25.18	36.93	37.29	38.88	45.61	36.41	36.58	34.37	46.14	66.90
TiO_2	0.06	0.09	1.49	0.26	0.00	0.10	0.08	0.07	1.55	0.34	0.00	0.11	0.09	0.04	0.05	0.32	0.06	0.00	0.00	0.04	0.59	0.01
Cr_2O_3	0.02	0.00	0.04	0.04	0.00	0.04	0.01	0.01	0.02	0.01	0.00	0.00	0.03	0.00	0.03	0.01	0.00	0.00	0.00	0.00	0.00	0.00
Al_2O_3	20.41	20.51	18.91	35.50	21.96	22.58	20.44	20.44	18.17	35.91	20.57	22.39	22.44	20.13	20.33	20.09	31.78	20.55	20.93	14.67	30.57	21.05
Fe_2O_3	1.12	1.13	0.00	0.00	0.00	0.00	0.67	0.66	0.00	0.00	0.00	0.00	0.00	0.60	0.30	0.00	4.85	0.58	0.40	0.00	3.56	0.04
FeO	31.53	35.76	20.88	1.13	0.02	27.16	26.89	33.41	22.66	1.14	0.06	28.30	27.93	9.01	10.82	9.33	0.41	21.81	23.67	24.13	2.01	0.00
MnO	5.15	0.51	0.05	0.00	0.00	0.03	6.65	1.01	0.05	0.00	0.00	0.08	0.06	29.65	26.80	0.77	0.04	19.91	17.84	0.26	0.09	0.03
MgO	1.08	2.30	9.21	0.50	0.00	13.46	0.76	1.48	7.88	0.54	0.00	12.92	12.99	1.48	2.52	15.45	1.04	0.12	0.12	5.24	0.70	0.00
CaO	3.55	2.78	0.04	0.00	2.68	0.04	7.67	6.25	0.03	0.04	1.33	0.03	0.02	1.97	1.70	0.30	0.03	0.95	1.30	0.83	0.00	2.07
Na_2O	0.11	0.01	0.16	1.95	10.36	0.00	0.05	0.03	0.18	1.68	10.95	0.01	0.00	0.00	0.00	0.21	0.57	0.03	0.03	0.25	0.25	10.73
K_2O	0.01	0.00	8.41	8.29	0.07	0.03	0.01	0.00	8.45	9.11	0.08	0.00	0.01	0.00	0.00	6.18	10.48	0.00	0.00	3.61	11.03	0.05
Total	99.56	99.80	95.25	94.65	101.48	88.78	100.85	101.12	95.02	95.54	101.04	88.83	88.75	99.81	99.83	91.53	94.87	100.37	100.87	83.39	94.94	100.87
Si	2.99	2.98	2.83	3.13	2.88	2.67	3.01	3.02	2.87	3.09	2.96	2.65	2.66	3.01	3.02	3.02	3.09	2.99	2.98	3.20	3.15	2.91
Ti	0.00	0.01	0.09	0.01	0.00	0.01	0.00	0.00	0.09	0.02	0.00	0.01	0.01	0.00	0.00	0.02	0.00	0.00	0.00	0.00	0.03	0.00
Cr	0.00	0.00	0.00	0.00	0.00	0.00	0.00	0.00	0.00	0.00	0.00	0.00	0.00	0.00	0.00	0.00	0.00	0.00	0.00	0.00	0.00	0.00
Al	1.97	1.96	1.75	2.79	1.12	2.80	1.93	1.92	1.70	2.79	1.05	2.79	2.80	1.93	1.94	1.84	2.54	1.99	2.01	1.61	2.46	1.08
Fe^{3+}	0.07	0.07	0.00	0.00	0.00	0.00	0.04	0.04	0.00	0.00	0.00	0.00	0.00	0.04	0.02	0.00	0.25	0.04	0.02	0.00	0.18	0.00
Fe^{2+}	2.16	2.43	1.37	0.06	0.00	2.39	1.80	2.23	1.51	0.06	0.00	2.50	2.47	0.61	0.73	0.61	0.02	1.50	1.61	1.88	0.11	0.00
Mn	0.36	0.04	0.00	0.00	0.00	0.00	0.45	0.07	0.00	0.00	0.00	0.01	0.01	2.05	1.84	0.05	0.00	1.38	1.23	0.02	0.01	0.00
Mg	0.13	0.00	1.08	0.05	0.00	2.11	0.09	0.18	0.93	0.05	0.00	2.04	2.05	0.18	0.30	1.79	0.11	0.01	0.01	0.73	0.07	0.00
Ca	0.31	0.28	0.00	0.00	0.12	0.00	0.66	0.54	0.00	0.00	0.06	0.00	0.00	0.17	0.15	0.02	0.00	0.08	0.11	0.08	0.00	0.10
Na	0.02	0.24	0.02	0.25	0.87	0.00	0.01	0.00	0.03	0.22	0.92	0.00	0.00	0.00	0.00	0.03	0.08	0.00	0.00	0.05	0.03	0.91
K	0.00	0.00	0.84	0.70	0.00	0.00	0.00	0.00	0.86	0.77	0.00	0.00	0.00	0.00	0.00	0.61	0.91	0.00	0.00	0.43	0.96	0.00
X_{Sps}	0.12	0.01					0.15	0.02						0.67	0.60			0.46	0.41			
X_{Alm}	0.73	0.81					0.60	0.74						0.20	0.24			0.50	0.55			
X_{Prp}	0.04	0.09					0.03	0.06						0.06	0.10			0.00	0.00			
X_{Grs}	0.11	0.08					0.22	0.18						0.06	0.05			0.03	0.04			
X_{Mg}	0.06	0.10	0.44			0.47	0.05	0.07	0.38			0.45	0.45	0.22	0.29	0.75		0.01	0.01	0.28		
X_{An}					0.12						0.06											0.10

and BA22, stilpnomelane (ad hoc model: Connolly [2005]) for samples BA23 and BA22, and spinel (White et al., 2002) for sample BA23.

For all four samples, an initial pseudosection was calculated using measured whole-rock major element compositions (Table S1), which were determined at Bureau Veritas Mineral Laboratories in Vancouver, Canada, and the Czech Geological Survey in Prague, Czech Republic. Pseudosections for samples BC43, BB11, and BA22 were calculated in a simplified MnNCKFMASHT system as they do not contain Fe^{3+}-rich phases. For these samples, Fe_2O_3 from whole-rock analysis was converted to FeO. Given abundant hematite and magnetite present in sample BA23, FeO and Fe_2O_3 concentrations were measured directly via titration, and pseudosections were calculated in the MnNCKFMASHTO system. For all pseudosections, H_2O was considered a saturated component. All samples contain accessory apatite, thus CaO corrections were applied based on measured P_2O_5 (except sample BB11, as discussed in Section 3.4.2).

Because garnet grains in samples BC43, BB11, and BA23 show strong compositional zoning (Figures 5a–5c), pseudosections calculated using effective bulk-rock compositions can only confidently estimate *P–T* conditions for garnet core growth (Evans, 2004). Thus, garnet fractionation routines were applied using PerpleX, where modeled garnet cores were subtracted from the bulk composition, and the resulting fractionated bulk compositions were used for further modeling. The starting conditions for garnet fractionation were estimated from the intersection of garnet endmember compositional isopleths from garnet cores. The end of the garnet fractionation path was estimated at the point when modeled garnet compositions most closely resembled measured rim values before the complete consumption of Mn from the bulk rock. As the actual P–T paths that the rocks followed are unknown, we chose to fractionate along linear gradients from surface conditions and intersect the garnet core estimates. Exploratory models using varying fractionation paths (not shown) revealed a negligible effect of the steepness of the slope on the composition of the fractionating garnet and the resulting bulk composition, thus suggesting that the chosen paths are adequate estimates. Pseudosections using the fractionated bulk rock compositions are presented with the pseudosections using measured bulk compositions. Fractionation routines were not conducted for sample BA22, as the garnet grains are small and only weakly zoned (Figure 5d).

3.4.1. Sample BC43

A pseudosection calculated for sample BC43 using measured bulk rock values (Figure 6a) shows modeled garnet core compositional isopleths for X_{Sps} (0.12 ± 0.01), X_{Alm} (0.73 ± 0.01) and X_{Grs} (0.11 ± 0.01) intersecting at ~540–550°C and 5.1–6.2 kbar. The X_{Prp} isopleths (0.03 ± 0.01) do not intersect, plotting at lower temperature conditions (Figure 6a). This inconsistency suggests that the analysis used for the garnet core composition is not from the exact center of the garnet, and/or implies problems with the bulk composition used for modeling (Evans, 2004). Despite this, the intersecting modal compositional isopleths provide an adequate estimate for garnet core *P–T* conditions.

After garnet fractionation, compositional isopleths for X_{Sps} (0.01 ± 0.01), X_{Grs} (0.08 ± 0.01), X_{Alm} (0.81 ± 0.01) and X_{Prp} (0.09 ± 0.01) intersect within error at 560–570°C and 5.5–6.5 kbar, within the phase-field containing the observed assemblage Pl + Chl + Grt + Ms + Pg + Ilm + Qz (Figure 6b). The model does not predict stable rutile; however, it is only present as inclusions in garnet and thus may have been stable during earlier growth, or reflect local compositional heterogeneity. Although the analyzed garnet rim compositions show good fit with the model, the compositional variables for biotite X_{Mg}, chlorite X_{Mg}, and plagioclase X_{An} do not exactly match the analyzed values (see Table 2). This either reflects issues with the solution models or indicates the re-equilibration of these minerals after the growth of the garnet. Despite these discrepancies, we consider the *P–T* conditions of 560–570°C and 5.5–6.5 kbar as best representing the estimate of peak metamorphic conditions for sample BC43.

3.4.2. Sample BB11

A pseudosection calculated for sample BB11 using the apatite-adjusted measured bulk rock composition shows garnet core isopleths for X_{Sps} (0.15 ± 0.01), X_{Alm} (0.60 ± 0.01), X_{Grs} (0.22 ± 0.01) and X_{Prp} (0.03 ± 0.01) intersecting at 510–520°C and 5.7–6.3 kbar (see Figure S1a). After garnet fractionation and modeling using the fractioned bulk composition, the resulting pseudosection showed poorly intersecting garnet compositional isopleths and garnet stability only within Pl-absent phase fields (see Figure S1b), suggesting that the modeled system was too CaO-poor. The measured bulk rock composition prior to apatite CaO adjustment already showed low CaO concentrations (Table S1), and plagioclase is only observed in trace amounts, indicating that small changes in CaO concentrations to the bulk composition can have a large effect on the model. It is likely that the initial

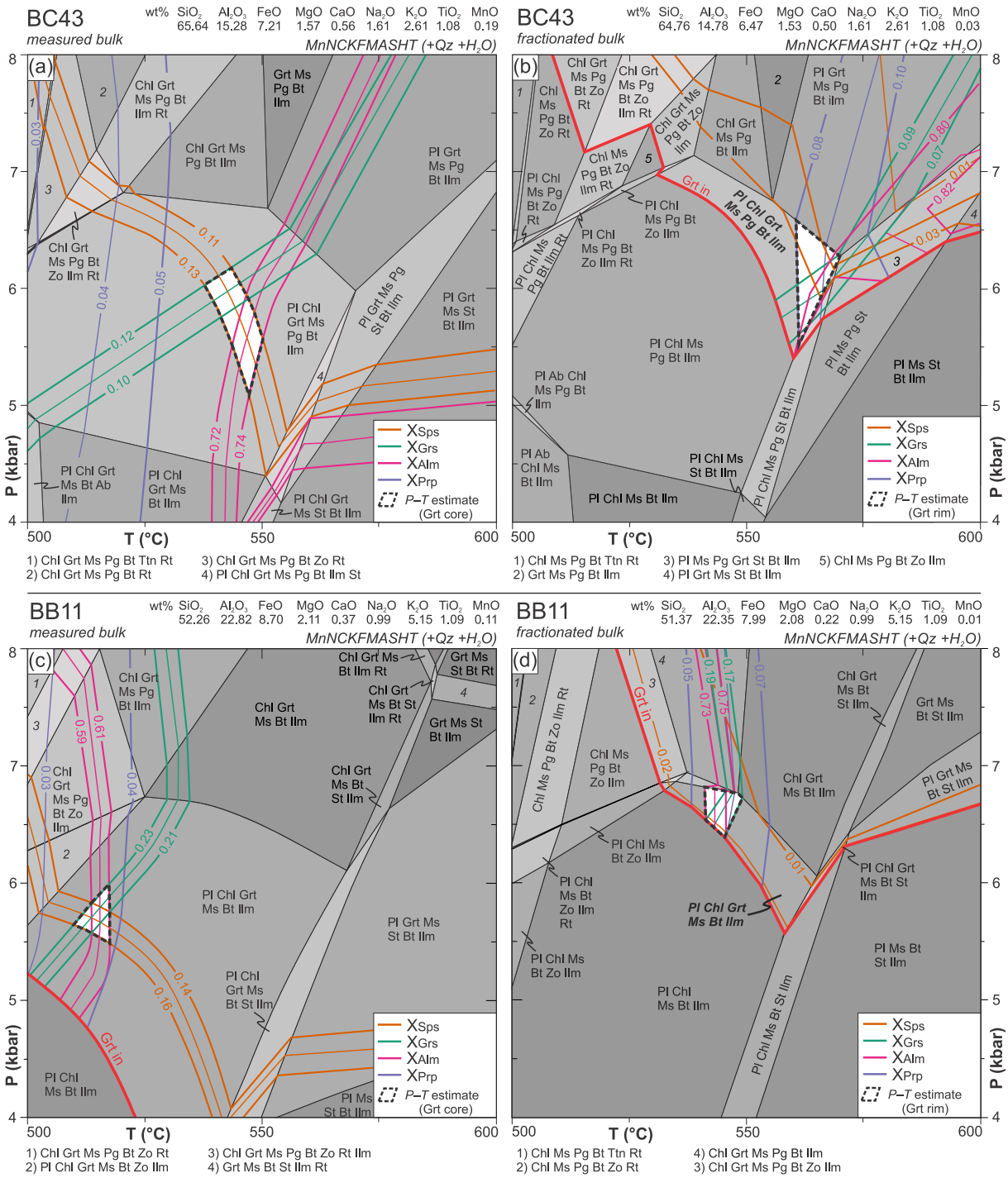

Figure 6. Pressure–temperature pseudosections calculated for: garnet–mica schist sample BC43 using (a) measured bulk composition and (b) estimated bulk composition after garnet fractionation calculations; garnet–mica schist sample BB11 using (c) measured bulk composition and (d) estimated bulk composition after garnet fractionation calculations. Higher variance fields are shown by darker shading. Contoured isopleths show observed compositional values with ±0.01 error. Fields containing the observed mineral assemblages are highlighted in bold and italics.

apatite adjustment removed too much CaO, and that the assumption that all measured P2O5 comes from apatite is incorrect, which is supported by the presence of monazite in the sample. Using the measured bulk-rock CaO concentration instead of the apatite-adjusted CaO resulted in a pseudosection with comparable phase fields, and the intersection of garnet core compositional isopleths at 510–520°C and 5.5–6.0 kbar (Figure 6c) matches

Table 2
Summary of Estimated P–T Conditions and Comparison of Observed Versus Modeled Mineral Compositional Parameters

	P–T estimates							Mineral modal compositions							
	T (°C)			P (kbar)											
	min	max	mean	min	max	mean		X_{Sps}	X_{Alm}	X_{Prp}	X_{Grs}	Grt X_{Mg}	Bt X_{Mg}	Chl X_{Mg}	X_{An}
BC43 core	540	550	545	5.1	6.2	5.7	obs.[a]	0.12	0.73	0.04	0.11	0.06	—	—	—
							mod.[b]	0.13	0.71	0.06	0.10	0.08	—	—	—
							diff.	−0.01	0.02	−0.02	0.01	−0.02	—	—	—
BC43 rim	560	570	565	5.5	6.5	6.0	obs.[a]	0.01	0.81	0.09	0.08	0.10	0.43	0.47	0.12
							mod.[b]	0.03	0.81	0.09	0.08	0.10	0.32	0.43	0.31
							diff.	−0.02	0.00	0.00	0.00	0.00	0.11	0.04	−0.19
BB11 core	510	520	515	5.5	6.0	5.8	obs.[a]	0.15	0.60	0.03	0.22	0.05	—	—	—
							mod.[b]	0.14	0.60	0.04	0.22	0.06	—	—	—
							diff.	0.01	0.00	−0.01	0.00	−0.01	—	—	—
BB11 rim	540	550	545	6.4	6.7	6.6	obs.[a]	0.02	0.74	0.06	0.18	0.07	0.40	0.43	0.07
							mod.[b]	0.02	0.76	0.06	0.17	0.07	0.25	0.38	0.38
							diff.	0.00	−0.02	0.00	0.01	0.00	0.15	0.05	−0.31
BA23 core (low-P range)	490	500	495	3.0	4.5	3.8	obs.[a]	0.67	0.21	0.06	0.06	0.22	—	—	—
							mod.[b]	0.69	0.20	0.03	0.05	0.22	—	—	—
							diff.	−0.02	0.01	0.03	0.01	0.00	—	—	—
BA23 rim	535	555	545	4.2	6.0	5.1	obs.[a]	0.60	0.24	0.10	0.05	0.29	0.74	—	—
							mod.[b]	0.59	0.27	0.10	0.01	0.31	0.72	—	—
							diff.	0.01	−0.03	0.00	0.04	−0.02	0.02	—	—
BA22	510	520	515	2.3	3.3	2.8	obs.[a]	0.43	0.53	0.00	0.04	0.01	0.29	—	0.10
							mod.[b]	0.40	0.52	0.04	0.03	0.08	0.25	—	0.19
							diff.	0.03	0.01	−0.04	0.01	−0.07	0.04	—	−0.09

[a]Representative compositional values of analyzed garnet (based on the rims and cores from transects across multiple grains), and biotite, chlorite and plagioclase (median value from multiple spot analyses). [b]Modeled mineral compositions at mean *P–T* conditions.

closely that from the CaO-adjusted model. After garnet fractionation (Figure 6d), garnet rim compositional isopleths for observed X_{Sps} (0.02 ± 0.01), X_{Grs} (0.18 ± 0.01), X_{Alm} (0.74 ± 0.01) and X_{Prp} (0.06 ± 0.01) intersect at 540–550°C and 6.4–6.7 kbar within a field containing the observed assemblage of Pl + Grt + Chl + Ms + Bt + Ilm + Qz, notably including plagioclase. Modeled compositional variables for biotite X_{Mg} and plagioclase X_{An} do not exactly match the observed values (see Table 2). Despite this, we consider this as best representing the peak metamorphic conditions for sample BB11.

3.4.3. Sample BA23

A pseudosection calculated for sample BA23 using the analyzed bulk-rock composition is presented in Figure 7a. Compositional isopleths for X_{Sps} (0.67 ± 0.01), X_{Mg} (0.21–0.23 ± 0.01), and X_{Grs} (0.05–0.06 ± 0.01) in garnet cores intersect between 475 and 500°C and 3–7 kbar (Figure 7a). Although the garnet isopleths do not allow for a precise pressure estimate, exploratory modeling (not shown) using garnet fractionation paths through the higher end of the pressure range, or with a steeper gradient not intersecting surface conditions, result in the destabilization of garnet before reaching the observed X_{Sps} compositional range, and the best-fit P–T path is through the lower end of this pressure estimate (3.0–4.5 kbar).– After garnet fractionation, isopleths for garnet X_{Sps} (0.60–0.62 ± 0.01) and X_{Mg} (0.29–0.30 ± 0.01), and biotite X_{Mg} (0.72–0.75) intersect within error at 535–555°C and 4.2–6.0 kbar within the phase-field containing the observed mineral assemblage of Chl + Grt + Ms + Bt + Mag + Hem + Rt (Figure 7b). Although the X_{Grs} isopleths (0.03–0.05 ± 0.01) do not intersect at this point, we still interpret this to be an adequate estimate of peak metamorphic conditions based on the intersection of the other compositional isopleths.

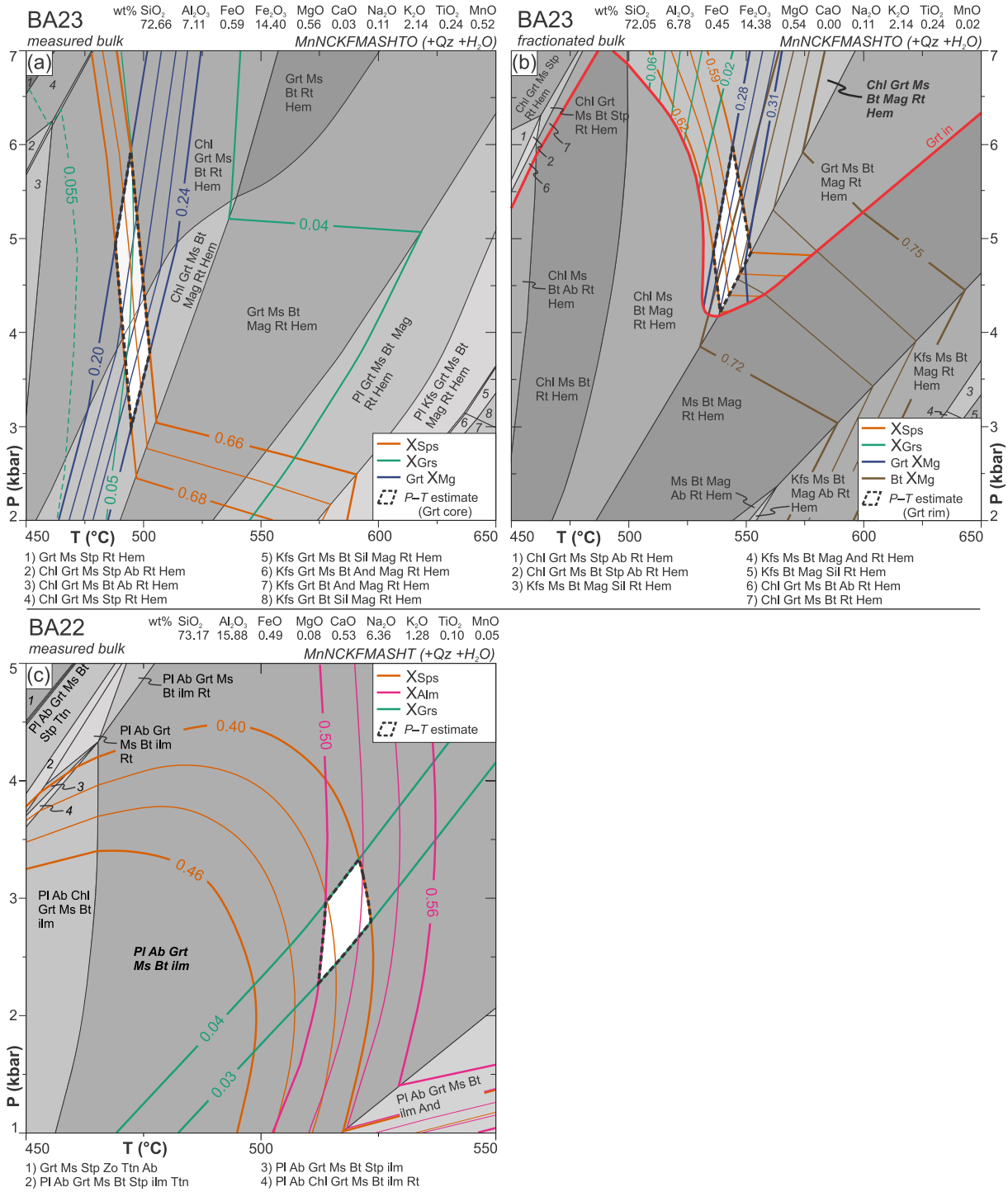

Figure 7. Pressure–temperature pseudosections calculated for: sample BA23 (garnet–mica schist) using (a) measured bulk composition and (b) estimated bulk composition after garnet fractionation calculations; (c) sample BA22 (felsic metavolcanic rock) using measured bulk composition. Contoured isopleths for sample BA23 show the observed compositional values with ±0.01 error, and for sample BA22 the entire range of garnet modal compositions are shown.

3.4.4. Sample BA22

The calculated pseudosection for sample BA22 shows the stability of the observed mineral assemblage (Pl + Ab + Grt + Ms + Bt + Ilm) over a large *P*–*T* range (Figure 7c). Modeled compositional variables for plagioclase X_{An} do not match observed values (see Table 2) and do not intersect with those for the garnet endmembers.

Table 3
Summary of Lu–Hf and Sm–Nd Dating Results

Sample	Fraction	Weight (mg)	Lu (ppm)	Hf (ppm)	$^{176}Lu/^{177}Hf$	$^{176}Hf/^{177}Hf$	Age (Ma)
BC43	Grt1	54.82	4.888	4.546	0.1521	0.283967 ± 3	652.5 ± 3.6
	Grt2	59.41	4.541	4.323	0.1486	0.283924 ± 3	
	Grt3	58.81	4.708	4.125	0.1614	0.284077 ± 3	
	WR	100.79	0.480	5.592	0.0121	0.282250 ± 4	
BB11	Grt1	41.65	5.249	0.211	3.5393	0.325075 ± 17	658 ± 38 (660.9 ± 2.3)[a]
	Grt2	51.64	5.260	0.183	4.1126	0.333191 ± 17	
	Grt3	52.83	6.642	0.213	4.4470	0.337321 ± 11	
	WR	99.56	0.531	3.452	0.0218	0.282465 ± 3	
BA23	Grt1	55.32	2.564	1.703	0.2130	0.284549 ± 4	649 ± 16
	Grt2	56.30	2.252	1.522	0.2093	0.284480 ± 3	
	Grt3	58.42	2.768	1.660	0.2359	0.284804 ± 4	
	WR	100.12	0.186	1.675	0.0157	0.282127 ± 4	
BA22	Grt1	71.08	10.912	1.178	1.3134	0.296635 ± 4	596.9 ± 1.7
	Grt2	70.87	10.629	1.246	1.2094	0.295529 ± 4	
	Grt3	76.35	10.567	1.098	1.3653	0.297305 ± 3	
	WR	100.98	0.034	3.628	0.0013	0.281980 ± 4	
Sample	Fraction	Weight (mg)	Sm (ppm)	Nd (ppm)	$^{147}Sm/^{144}Nd$	$^{143}Nd/^{144}Nd$	Age (Ma)
BC43	Grt1	54.82	2.291	1.177	1.1778	0.516243 ± 10	647 ± 10
	Grt2	59.41	2.262	0.949	1.4422	0.517368 ± 15	
	Grt3	58.81	2.314	1.008	1.3901	0.517177 ± 13	
	WR	100.79	2.414	39.145	0.1299	0.511816 ± 04	

Note. All errors are 2 SE (standard errors) and relate to the last significant digits. 176Lu/177Hf errors are 0.5% and $^{147}Sm/^{144}Nd$ errors are 0.3%. JMC475 yielded $^{176}Hf/^{177}Hf = 0.282163 \pm 6$ ($n = 8$) and JNd-1 gave $^{143}Nd/^{144}Nd = 0.512090 \pm 10$ ($n = 6$) over the period of analyses. Mass bias corrections conducted using $^{179}Hf/^{177}Hf = 0.7325$ and $^{146}Nd/^{144}Nd = 0.7129$. Decay constants used for age calculations: $\lambda_{176Lu} = 1.865 \times 10^{-11}$ yr^{-1} (Scherer et al., 2001) and $\lambda_{147Sm} = 6.02 \times 10^{-12}$ $year^{-1}$ (Lugmair & Marti, 1978). Age uncertainties are 2σ.
[a]Age calculated with three-point isochron excluding Grt1.

However, garnet compositional isopleths for X_{Sps} (0.40–0.46), X_{Alm} (0.50–0.56), and X_{Grs} (0.03–0.04) intersect at 510–520°C and 2.3–3.3 kbar, which we interpret as the best estimate of *P–T* conditions for garnet growth.

3.5. Garnet Lu–Hf and Sm–Nd Geochronology and Trace Element Chemistry

The results of garnet Lu–Hf and Sm–Nd isotopic dating and trace element analysis are summarized in Table 3 and Figure 8 and presented in Data Set S2. Sample preparation and mass spectrometry procedures are summarized in Anczkiewicz et al. (2004) and Anczkiewicz and Thirlwall (2003). Standards reproducibility and constants used for the calculations are given in the footnote to Table 3. Four samples were analyzed by isotope dilution, each producing a Lu–Hf isochron from two to three garnet aliquots and one representative whole rock powder. One sample further produced a Sm–Nd isochron from three garnet aliquots and one whole rock powder. We obtained Lu–Hf isochron ages of 652.5 ± 3.6 Ma, 660.0 ± 2.3 Ma, 649 ± 16 Ma, and 596.9 ± 1.7 Ma for samples BC43, BB11, BA23, and BA22, respectively (Figures 8a–8d), and a Sm–Nd isochron age of 647 ± 10 Ma for sample BC43 (Figure 8e). One garnet fraction was rejected from sample BB11 (Grt1, see Section 4.1.1).

Trace elements were analyzed along rim-to-rim transects across representative garnets from each sample to determine the potential influence of inclusions on bulk mineral separate isotopic systematics, and the influence of zonation on age interpretation. The analytical methods are presented Text S1 in Supporting Information S1. A summary of the results is presented in Figures 8f–8j and the full dataset can be found in Data Set S3. The apparatus and analytical protocols are provided in Anczkiewicz et al. (2012). We used NIST 612 glass as a primary

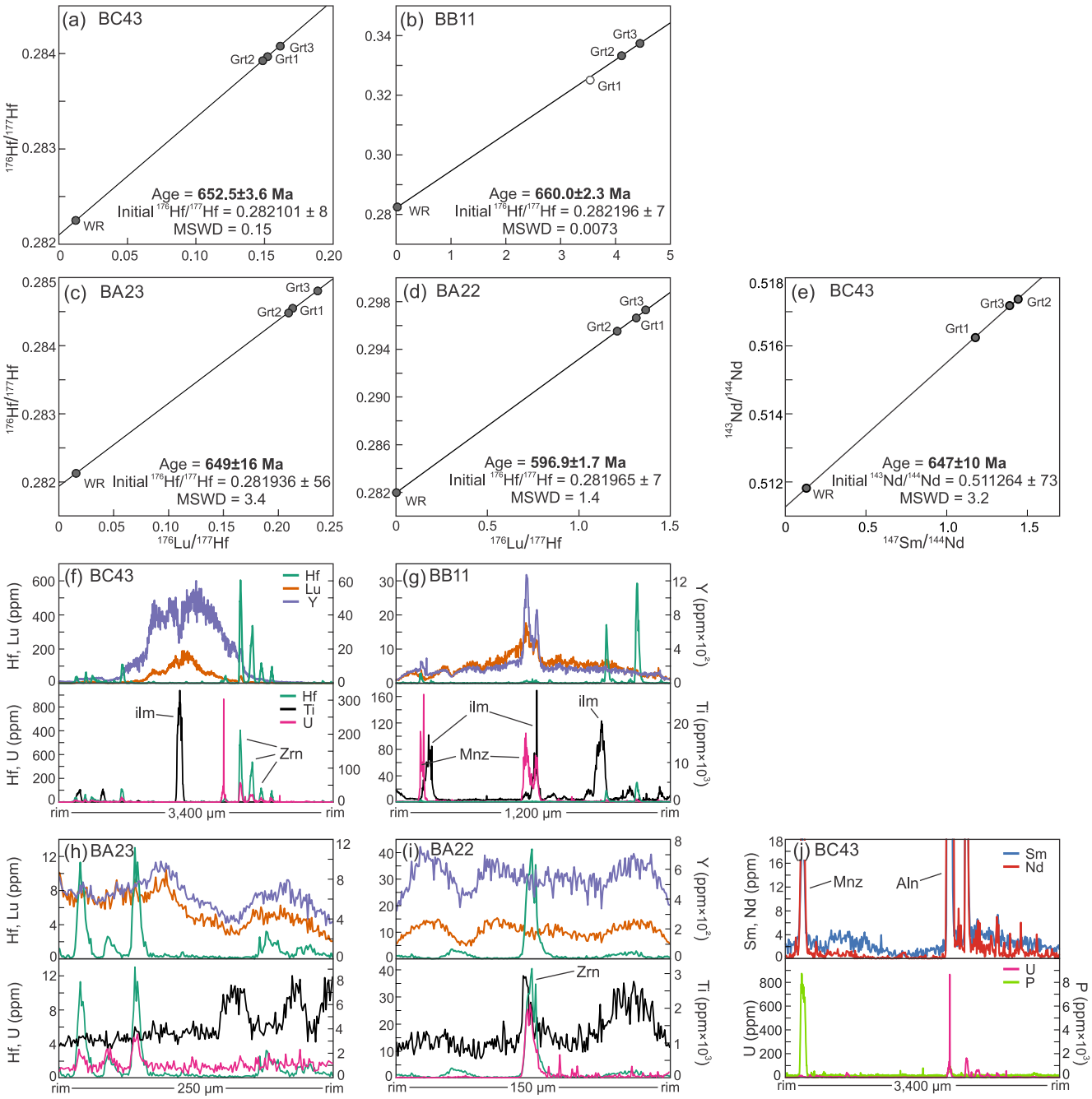

Figure 8. Results of Lu–Hf and Sm–Nd dating, and trace element analysis. (a)–(d) Lu–Hf isochron plots (open circle in (b) represents the rejected aliquot for BB11 that was not considered in the isochron). (e) Sm–Nd isochron plot for sample BC43. (f)–(i) Element distribution profiles of Hf, Lu, Y, Ti and U, measured across representative garnet grains. (j) Element distribution profile of Sm, Nd, U and P, measured across the same grain from sample BC43.

standard and BCR2G glass was measured for quality control. GEOREM recommended values were applied (Jochum et al., 2011, 2016).

In sample BC43, Lu is strongly enriched in garnet cores and decreases sharply toward the rims (Figure 8f), and Sm and Nd show the opposite trend with enrichment away from the core (Figure 8j), which is consistent with Rayleigh fractionation during garnet growth (Hollister, 1966). Large peaks in the Sm and Nd profiles correspond to inclusions of accessory minerals such as monazite and allanite. Garnet grains from sample BB11 show Lu-enriched cores and depleted rims (Figure 8g), although concentrations are significantly lower than sample BC43.

Samples BA23 and BA22 have similar Lu concentrations to sample BB11 but show flatter Lu zonation with no systematic variation from core to the rim (Figures 8h and 8i). In all four samples, the average concentration of Hf in clean parts of the garnet (without mixed analyses from mineral inclusions) is generally around 0.2 ppm and does not vary significantly across or between grains. Peaks in Hf and Zr correspond to inclusions of zircon, which is further discussed in Section 4.1.

3.6. Monazite U–Pb Geochronology and Trace Element Chemistry

To complement garnet Lu–Hf and Sm–Nd ages, monazite grains from sample BC43 were separated and analyzed for trace elements and dated by U–Pb LA–ICP–MS method, with the results presented in Figure 9. A Thermo Scientific Element 2 sector field ICP-MS coupled to a 193 nm ArF excimer laser (Teledyne CETAC Analyte Excite laser), at the Institute of Geology of the Czech Academy of Sciences, was used to measure the Pb/U, Pb/Th, and Pb isotopic ratios, and rare earth element and Y (REE + Y) concentrations in monazite. Details of the mineral separation procedures are provided in Supporting Information Text S1, and the analytical details and results are provided in Data Sets S4 and S5.

Trace element composition maps of representative monazite grains show some zoning/variation across individual grains (Figures 9a and 9b). Chondrite-normalized REE patterns (Figure 9c) show a typical monazite REE distribution pattern with decreasing concentration from the light to the heavy REEs, and all grains show a negative Eu-anomaly. The REE patterns show two distinct groups, with one group showing a significantly higher HREE concentration of at least one order of magnitude (Figure 9c).

From U–Pb analysis of 6 grains, two age groups were identified corresponding to the two trace element patterns (Figure 9d). Analysis of four spots from one grain showing the high-HREE pattern yielded a combined concordia age of 583.9 ± 8.0 Ma (2σ, MSWD = 0.24; Figure 9b). From the analysis of 14 spots in five grains showing the low-HREE pattern, 12 yielded concordant dates that combined to give a $^{207}Pb/^{235}U$–$^{206}Pb/^{238}U$ concordia age of 640.9 ± 7.0 Ma (95% conf., MSWD = 11.4; Figure 9c).

3.7. $^{40}Ar/^{39}Ar$ Mica Geochronology

Four samples were selected for $^{40}Ar/^{39}Ar$ geochronology of biotite (sample BC43) and muscovite (samples JBD14, BC30, and JBD09). Biotite was separated and analyzed from sample BC43 with the intention of constraining the timing of exhumation of the S_1 fabric prior to F_2 folding, as this sample represents part of the medium-grade zone showing very little S_2 overprint (Region 1; Figure 2a). Two samples were collected from high-strain zones within the Brusque Complex to constrain the timing of deformation associated with the development of the S_2 fabric (JBD14 and BC30, Figure 1c). The muscovite in these samples consists of neocrystallized grains lying parallel to the overprinting S_2 fabric (e.g., Figure 4c). One sample was collected from a high-strain zone within the Itajaí–Perimbó Shear Zone (JBD09, Figure 1c) to constrain the timing of movement along the northern boundary of the Brusque Complex. Details of sample preparation and analytical methods are provided Text S1 in Supporting Information S1.

The results from $^{40}Ar/^{39}Ar$ analysis of biotite and muscovite are presented in Figure 10. Five heating steps for biotite from sample BC43 released ~50% ^{39}Ar and defines a plateau age of 635 ± 4 Ma (MSWD = 0.93; Figure 10a). Ten heating steps on muscovite from sample JBD14 released ~80% ^{39}Ar, defining a plateau age of 601 ± 9 Ma (MSWD = 0.70; Figure 10b). Thirteen heating steps on muscovite from sample BC30 released ~85% ^{39}Ar and defines a plateau age of 571 ± 3 Ma (MSWD = 0.28; Figure 10c). Five heating steps for muscovite from sample JBD09 released ~60% ^{39}Ar and defines a plateau age of 545 ± 4 Ma (MSWD = 1.55; Figure 10d). Complete results and analytical details are presented in Supplementary Information Data Set S6.

4. Discussion

4.1. Interpretation of Geochronological Results

4.1.1. Lu–Hf and Sm–Nd Garnet Ages and Their Meaning

Garnet analyzed by isotopic dilution in samples BC43 and BA23 shows Hf concentrations between 4.13–4.55 and 1.52–1.70 ppm, respectively (Table 3), which is considered high for garnet in typical metamorphic rocks

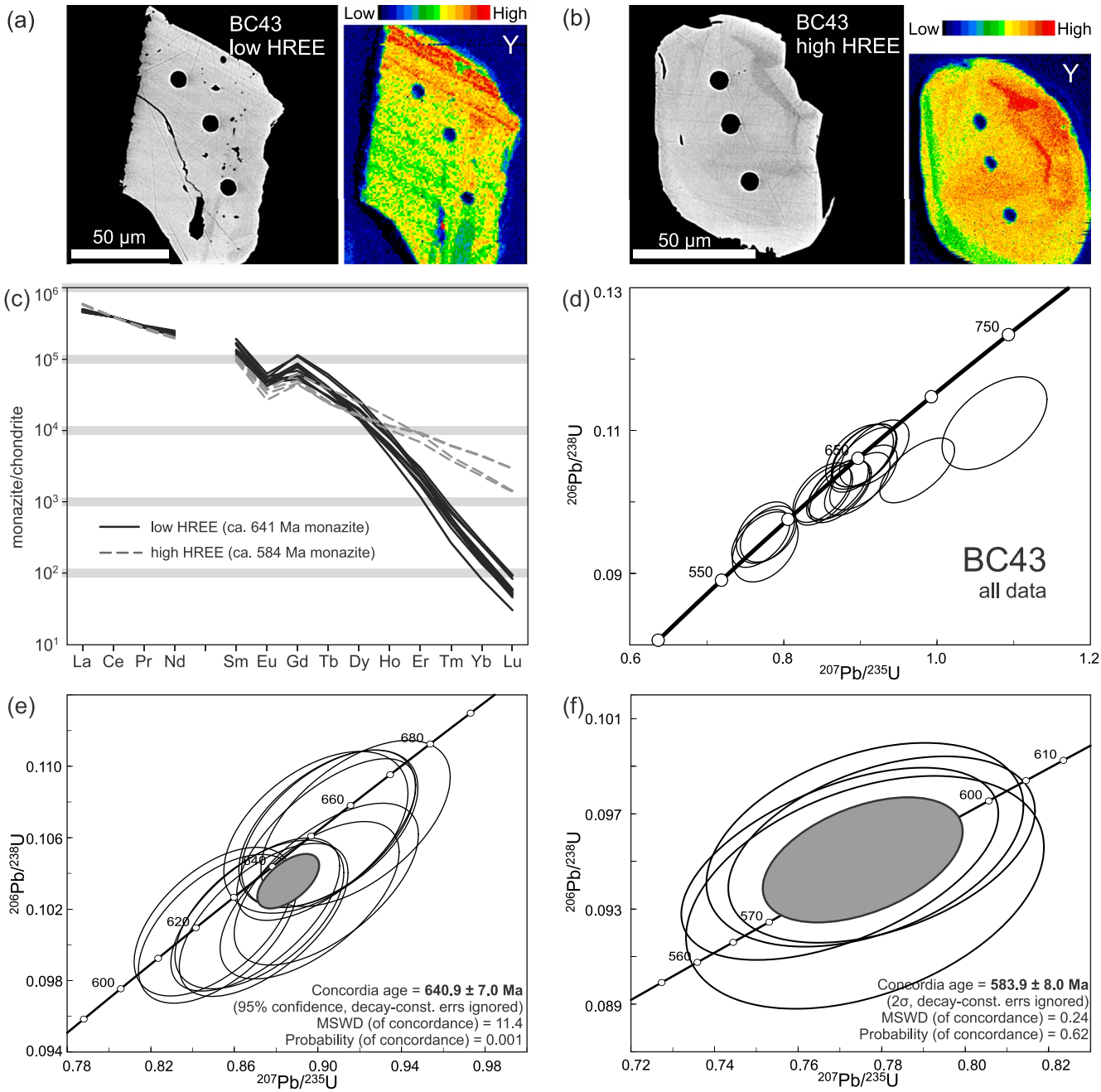

Figure 9. Results of trace element analysis and U–Pb dating (data-point error ellipses are 2σ) of monazite from sample BC43. (a–b) Monazite BSE images and yttrium compositional maps for representative grains from the two age groups. (c) Chondrite-normalised monazite REE plot (after McDonough & Sun, 1995). (d) Concordia diagram showing all monazite U–Pb data. (e) Detail of ca. 640 Ma analyses (ignoring discordant data) and concordia age. (f) Detail of ca. 580 Ma analyses and concordia age.

(Anczkiewicz et al., 2014; Cheng, 2019; Scherer et al., 2000). This is significantly higher than results obtained by LA-ICP-MS analysis from inclusion-free parts of individual garnet porphyroblasts, which show Hf concentrations between ~0.05 and 0.40 ppm for both samples. In contrast, garnet isotope dilution of sample BB11 shows Hf concentrations ~0.2 ppm (Table 3), which is comparable to estimates from LA-ICP-MS analysis of between ~0.05 and 0.10 ppm. This disparity between measured Hf concentrations is likely attributed to contamination from Hf-rich accessory mineral inclusions in garnet, such as ilmenite, rutile, and possibly zircon. The presence of sub-micron inclusions of zircon in garnet is confirmed from all four samples by corresponding spikes

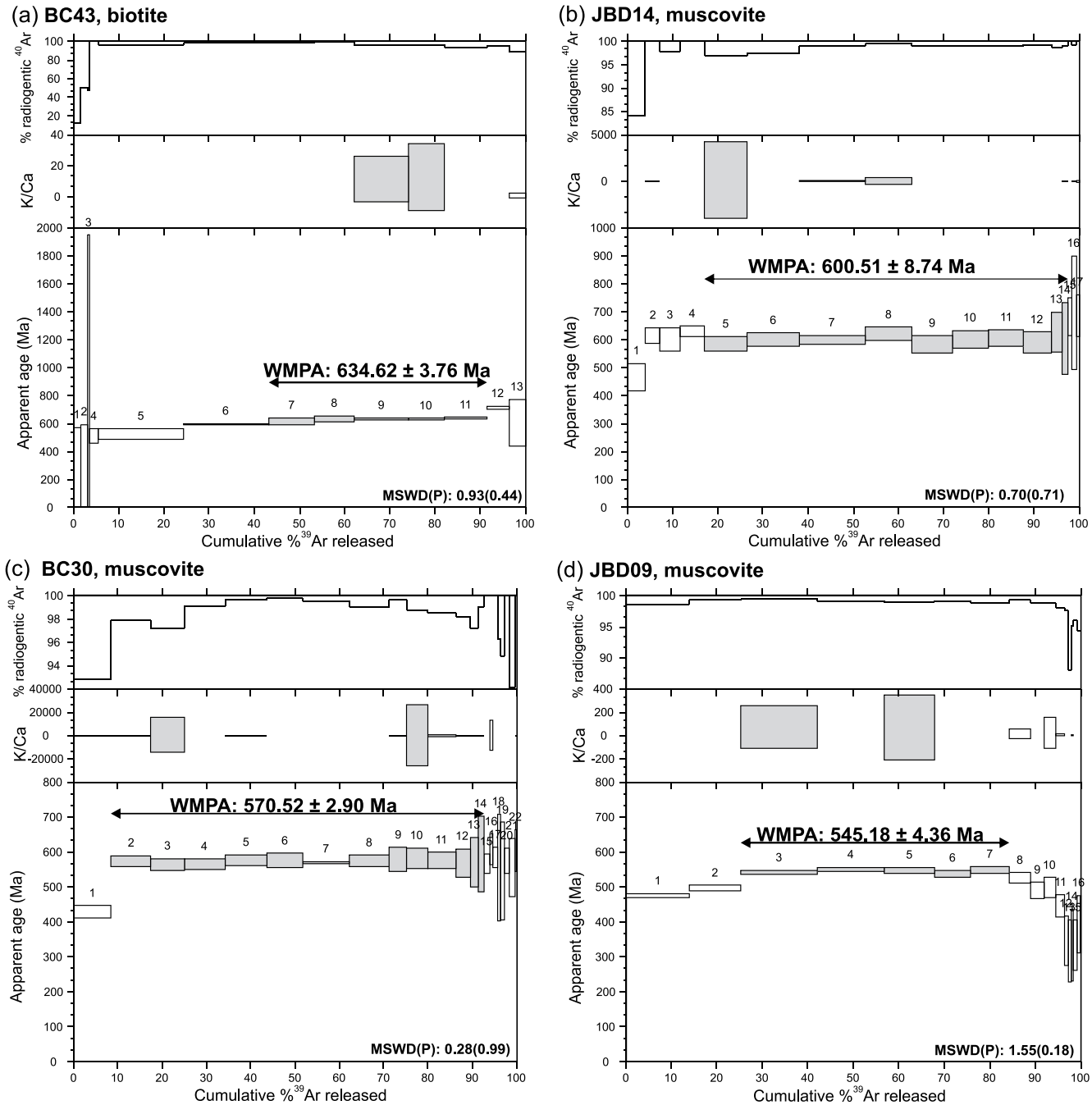

Figure 10. Mica $^{40}Ar/^{39}Ar$ spectra. (a) Biotite from sample BC43 from the medium-grade Brusque Complex. (b) Muscovite from sample JBD14 from a high-strain zone (S_2) within the low-grade Brusque Complex. (c) Muscovite from sample BC30 from a high-strain zone (S_2) within the low-grade Brusque Complex. (d) Muscovite from sample JBD09 from a mylonitic part of the Morro do Parapente Granite within the Itajaí–Perimbó Shear Zone.

in U and Hf (Figures 8f–8i), and the presence of ilmenite is obvious from petrographic observations. Despite efforts to reduce the presence of such inclusions in garnet aliquots through manual picking and hotplate dissolution (after Anczkiewicz et al., 2004), the high total Hf and low $^{176}Lu/^{177}Hf$ ratios in samples BC43 and BA23 (Table 3) indicate that some Hf-rich phases were dissolved with the garnet. In contrast, sample BB11 shows a good match between Hf concentrations as measured by isotope dilution (0.18–0.21ppm) and LA-ICP-MS (~0.2 ppm), suggesting such high-Hf inclusions were successfully excluded from the analysis.

Although sample BC43 shows significant Hf contamination and low $^{176}Lu/^{177}Hf$ ratios, the high age precision (652.5 ± 3.6 Ma; Figure 8a) and good regression line (MSWD = 0.15) indicates low scatter between analyses, suggesting that Hf contamination did not greatly affect the analyses. The poor age precision from sample BA23 (649 ± 16 Ma; Figure 8c), however, is likely due to low $^{176}Lu/^{177}Hf$ ratios resulting from contamination by Hf-rich mineral inclusions disparately affecting the individual garnet fractions. In contrast, due to the low total Hf and high $^{176}Lu/^{177}Hf$ ratios measured by isotope dilution of sample BB11 (Table 3), the poor precision of the resulting isochron age is likely due to problems with the outlying data point *Grt1*. This garnet fraction (*Grt1*) was prepared separately from the other two (*Grt2* and *Grt3*) and was subjected to much less rigorous purification by mechanical picking. For this reason, a three-point isochron excluding *Grt1* has been calculated for sample BB11, which gives a more precise age of 660.0 ± 2.3 Ma (Figure 8b).

If there is a significant contribution of Hf from detrital zircon in the isotope dilution analyses, our calculated isochron ages may be skewed from their true ages (Scherer et al., 2000). This type of contamination may be responsible for the disparity between the Lu–Hf ages from samples BC43 and BA23 (ca. 650 Ma) compared with sample BB11 (ca.660 Ma), the latter of which shows little to no evidence of Hf contamination. However, these calculated isochron ages lie relatively close together (within error), and thus it is unlikely that contamination by high-Hf mineral inclusions greatly affected their accuracy. This suggests that Hf-rich mineral phases that were in equilibrium with garnets, such as ilmenite, rutile, and metamorphic zircon, were responsible for Hf contamination, and detrital zircon grains were successfully removed during sample preparation.

Isotope dilution analysis from sample BA22 shows Hf concentrations in garnet between ~1.10 and 1.25 ppm (Table 3), which is higher than estimates from LA-ICP-MS analysis of ~0.1–0.3 ppm, thus suggesting a small amount of Hf contamination. However, considering the high $^{176}Lu/^{177}Hf$ ratios obtained by isotope dilution analysis (Table 3), Hf contamination likely came from inclusions of mineral phases with low-Hf concentrations such as primary metamorphic feldspar (Figure 8f).

Lu concentrations measured by isotope dilution from all garnet samples (Table 3) correspond well with values as determined by LA-ICP-MS (Figures 8f–8i). Garnet from samples BC43 and BB11 show Lu- and Y-zoning typical of Rayleigh fractionation during prograde growth, with the highest concentrations in the cores and decreasing toward the rims (Figures 8f and 8g). Prograde garnet growth is also indicated by major element profiles and pseudosection models, and thus we interpret the ages of 652.5 ± 3.6 and 660.0 ± 2.3 Ma from samples BC43 and BB11, respectively, as recording the timing of early prograde garnet growth in the Brusque Complex. The relatively flat Sm–Nd profiles in garnet from sample BC43 (Figure 8j) are similarly consistent with Rayleigh-type fractionation during prograde growth (e.g., Lapen et al., 2003), and indicate that the 647 ± 10 Ma Sm–Nd age likely reflects and average growth age, although the lowest Sm and Nd concentrations in garnet cores suggest it may be slightly biased toward later growth. Thus, the overlap of the Lu–Hf and Sm–Nd ages from sample BC43 suggests that garnet growth was brief, consistent with published estimates of growth duration in medium-grade metapelites (Anczkiewicz et al., 2014; Pollington & Baxter, 2010; Schmidt et al., 2015; Vance & Keith O'Nions, 1992).

Garnet porphyroblasts from samples BA23 and BA22 show mostly flat Lu and Y profiles across garnet grains, with little core–rim variation (Figures 8h and 8i). Although the major element zonation profiles from these samples preserve prograde garnet growth (Figures 5c and 5d), the small grain size (<0.25 mm) indicates possible Lu–Hf diffusion during growth despite the relatively low temperatures of ~540°C (Scherer et al., 2000), which may account for the flat Lu and Y profiles. Based on this, we interpret the ages of 649 ± 16 and 596.9 ± 1.7 Ma from samples BA23 and BA22, respectively, as average ages of garnet growth.

4.1.2. U–Pb Monazite Ages and Their Meaning

The 641 ± 8 Ma U–Pb monazite age obtained from sample BC43 shows both poor MSWD and probability of concordance, likely reflecting the low sample size (Figure 9c). Despite this, the age overlaps within error with the ca. 647 ± 10 Ma garnet Sm-Nd isochron age, supporting the coeval growth of monazite and garnet. To test if monazite and garnet grew in equilibrium, we have calculated the apparent monazite/garnet REE distribution coefficients for sample BC43 and compared the results against previously published reference values (Hermann & Rubatto, 2003; Rubatto et al., 2006; Warren et al., 2018). Recent studies have urged for caution when using monazite–garnet partition coefficients from natural samples as evidence of growth in equilibrium (Hagen-Peter et al., 2016; Warren et al., 2018), and there is evidence to suggest that REE partitioning between monazite

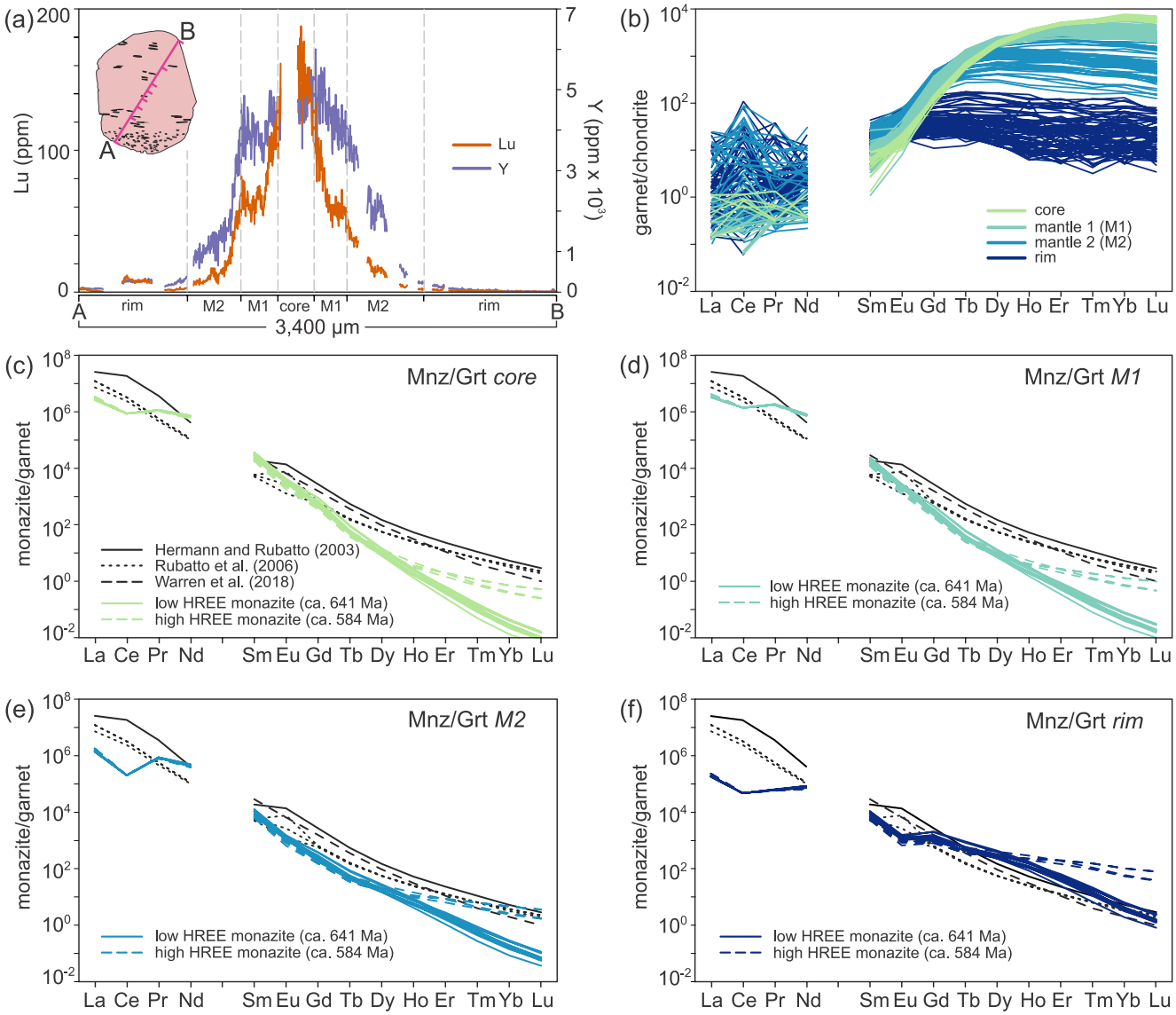

Figure 11. (a) Distribution of Y and Lu across a representative garnet grain from sample BC43, with zoning defining a core, mantle 1 (M1), mantle 2 (M2), and rim. (b) Chondrite-normalised rare earth element (REE) plot showing variation from core to rim in the same garnet grain (reference values from McDonough & Sun, 1995). (c)–(f) Apparent garnet/monazite REE distribution coefficients for garnet cores, M1, M2, and rims, compared with known published data (Hermann & Rubatto, 2003; Rubatto et al., 2006; Warren et al., 2018). The apparent partition coefficients were calculated using individual monazite REE analyses against averages of each garnet zone.

and garnet is temperature-dependent (Warren et al., 2018). However, partitioning values do not appear to differ greatly between sub- and supra-solidus metapelites (Hermann & Rubatto, 2003; Rubatto et al., 2006; Warren et al., 2018).

Due to the core–rim compositional variation in garnet, apparent distribution coefficients were calculated using average values measured from four zones identified in a representative garnet grain from sample BC43. In this grain, a plateau in HREE + Y concentration in the mantle was used to define two separate mantle zones, referred to as mantle 1 (M1) and mantle 2 (M2), in addition to core and rim zones (Figures 11a and 11b). The results show that none of the apparent partition coefficients calculated for the high HREE (ca. 584 Ma) monazite match the reference values (Figures 11c–11f). The distribution curves, like the chondrite-normalized REE plots (Figure 9d), show much higher HREE concentrations compared to the older grains, likely reflecting the dissolution of an HREE-rich phase, such as garnet, prior to or at ca. 584 Ma. Because of this, we interpret the ca. 584 Ma monazite as recording a minor retrograde event.

The apparent partition coefficients calculated for the low HREE (ca. 641 Ma) monazite and garnet core, M1, and M2 zones similarly show a poor fit, plotting well below the reference values (Figures 11c–11e). However, the apparent HREE partition coefficients calculated for garnet rims show a good fit with (Figures 11f), indicating that the ca. 641 Ma monazite likely grew in equilibrium with garnet rims. These observations confirm the coeval growth of monazite and garnet rims, which we interpret to support that peak regional metamorphism in sample BC43 was reached ca. 645–640 Ma.

4.1.3. Ar–Ar Ages and Their Meaning

Microstructural observations of sample BC43 show biotite to have crystallized during the development of S_1 and estimates from thermodynamic modeling place the peak metamorphic conditions experienced by this sample upwards of ~570°C (Figure 6b). Considering that the calculated bulk closure temperature of biotite of similar size and composition to that analyzed in sample BC43 is ~300 ± 50°C (Grove & Harrison, 1996), the biotite $^{40}Ar/^{39}Ar$ age of 635 ± 4 Ma (Figure 10a) likely represents a cooling age. However, the step heating experiment shows an almost staircase pattern which could point to a mixture with a relict Ar-reservoir partly escaping outgassing (Bosse & Villa, 2019) or excess Ar not resolved through analysis, thus it is possible this does not represent a pure cooling age.

The three muscovite samples—JBD14, BC30, and JBD09—were collected from rocks showing clear S_2 overprint, and each sample yielded much younger $^{40}Ar/^{39}Ar$ ages compared to sample BC43, between ca. 600 and 545 Ma (Figures 10b–10d). Although we have not obtained reliable temperature constraints for these samples, the mineral assemblages suggest lower-greenschist facies conditions, and the predominance of bulging recrystallization of quartz suggests maximum temperatures of ~400°C. These conditions are approximately at or below the bulk closure temperature of Ar in muscovite of similar size, at ~400°C (Harrison et al., 2009), suggesting that these ages likely reflect the timing of (re) crystallization of synkinematic muscovite.

Based on these observations, we interpret the ca. 635 Ma biotite $^{40}Ar/^{39}Ar$ age yielded from sample BC43 as the timing of cooling of the Brusque Complex within S_1 driven by thrust-controlled exhumation, whereas the muscovite $^{40}Ar/^{39}Ar$ ages reflect reworking of the flat S_1 foliation by the S_2 fabric. The muscovite ages within the center of the complex (ca. 600 and 585 Ma) coincide with the timing of granite intrusion between ca. 615–585 Ma (Hueck et al., 2019). These intrusions likely provided heat and fluids for the re-equilibration/recrystallization of the muscovite during reworking of the S_1 fabric.

4.2. Tectono-Metamorphic Evolution of the Northern Dom Feliciano Belt

4.2.1. Early Crustal Thickening and Peak Regional Metamorphism (Ca. 660 to 640 Ma)

The earliest structural feature preserved in the Brusque Complex is the pervasive, flat-lying metamorphic S_1 foliation. The foliation contains intrafolial folds suggestive of development during progressive simple shearing, and the NW–SE-trending L_1 stretching lineations and associated kinematic indicators indicate that it developed during low-angle NW-directed shearing. As S_1 is the earliest major structure recognized in the complex, it likely developed during early convergence, which is consistent with interpretations from previous studies (e.g., Basei et al., 2011; De Toni, Bitencourt, Konopásek, et al., 2020). This further suggests that S_1 originally dipped shallowly toward the SE, and the local reorientation of S_1 in Region 1 may be the result of doming after intrusion of the Valsungana Batholith.

Phase equilibria modeling of the medium-grade Brusque Complex metasedimentary rocks suggests that prograde garnet growth culminated at 540–570°C and 5.5–6.7 kbar, corresponding to an apparent geothermal gradient of ~25°C/km (Figure 12) that is consistent with regional orogenic metamorphism within a medium P/T series typical for crustal thickening (Winter, 2014). The randomly oriented, equidimensional mineral inclusions found in some garnet cores (Figures 5a and 5b), together with the oriented inclusions continuous with S_1 found in the majority of garnet, suggests pre-to syn-kinematic garnet growth during S_1 development (Zwart, 1962). Thus, based on the Lu–Hf garnet geochronology from this study, crustal thickening due to progressive thrusting in the Dom Feliciano Belt foreland was likely underway by ca. 660–650 Ma. This corresponds with the timing of convergence and crustal thickening in the hinterland estimated from early melting in the Porto Belo Complex (Chemale et al., 2012; De Toni, Bitencourt, Konopásek, et al., 2020; De Toni, Bitencourt, Nardi, et al., 2020;

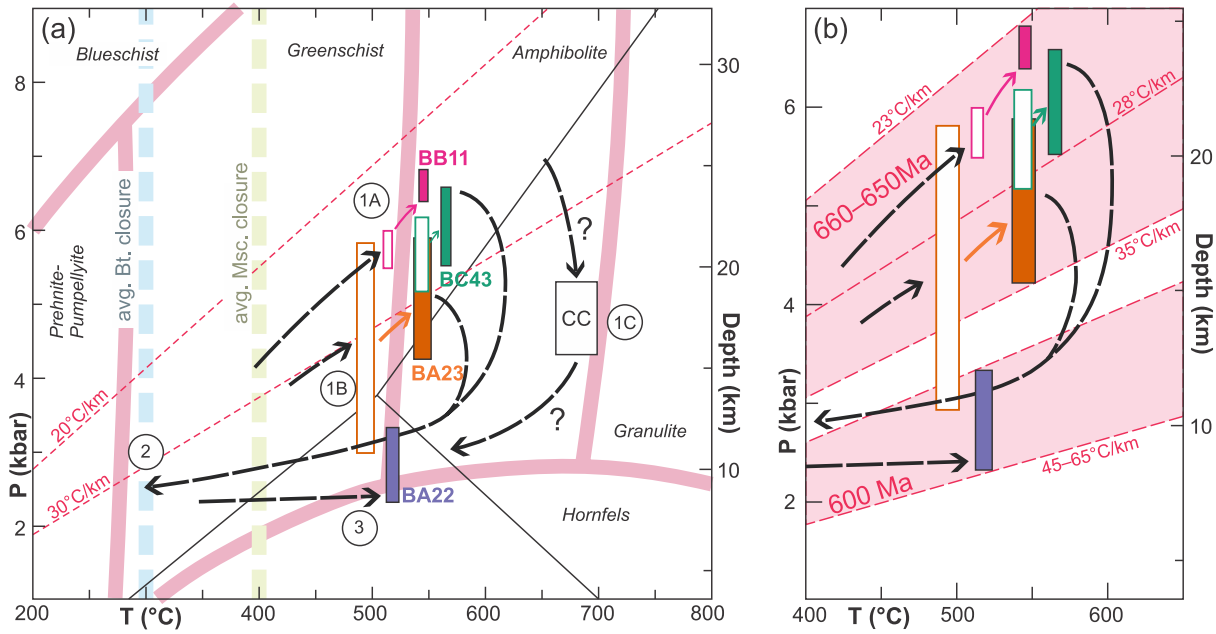

Figure 12. (a) Summary of P–T–t data. Estimated P–T paths (dashed lines and arrows) show a clockwise evolution. Open and filled rectangles show P–T estimates using measured and fractionated bulk rock compositions, respectively. Depth is calculated using an average crustal density of 2.8 g/cm^3. 1A = increasing P–T during early crustal thickening and prograde garnet growth between ca. 660–650 Ma; 1B = increasing thermal gradient during progressive thrusting at ca. 650 Ma; 1C = further heating and decompressive melting in the basement (CC – Camboriú Complex) after the end of thrusting (De Toni, Bitencourt, Konopásek, et al., 2020); 2 = cooling of Brusque Complex between ca. 635–615 Ma; 3 = granite intrusion into the Brusque Complex and contact metamorphism by at least ca. 600 Ma. (b) Detail of P–T estimates showing increasing apparent thermal gradients in the foreland from ca. 660 to 600 Ma related to intrusion of granitoids from ca. 630 Ma.

Hueck, Basei, et al., 2018). The complex reached a regional metamorphic peak between ca. 650–640 Ma, as constrained by garnet Sm–Nd and monazite U–Pb dating.

P–T estimates from sample BA23 in the southern, low-grade part of the Brusque Complex indicate peak regional metamorphic conditions at lower amphibolite facies, between 535 and 555°C and 4.2–6.0 kbar (Figure 12a). The lower end of the pressure estimate suggests peak regional metamorphism at a higher crustal position compared to the medium-grade domain, corresponding to a maximum apparent geothermal gradient of ~35°C/km (Figure 12b). Although this part of the complex is dominated by low-grade, greenschist-facies rocks, these results, and the few relict garnet-bearing outcrops observed in the field, suggest that at least parts of this region may be retrogressed equivalents to the central medium-grade domain. The 649 ± 16 Ma metamorphic age yielded from this sample is within error of those from the two medium-grade metapelites, however, the lower pressure conditions and higher apparent thermal gradient suggests that this rock may record a slightly later stage of orogenesis related to increasing thermal input during thrusting in the foreland. This is consistent with thermal relaxation during crustal thickening after burial beneath the hinterland between ca. 660–650 Ma.

4.2.2. Exhumation and Progressive Switch to Partitioned Transpression (Ca. 635 to 615 Ma)

The Ar–Ar biotite age from sample BC43 indicates that at least the uppermost parts of the Brusque Complex cooled to ~300°C by ca. 635 Ma, suggesting thrust-controlled partial exhumation of the complex by this time (Figure 12a). Due to the staircase-like step heating pattern (Figure 10a), however, 300°C is considered the minimum cooling temperature (Bosse & Villa, 2019), and as the ending of thrust-controlled exhumation of the foreland is only constrained by this one data point, we consider it a maximum age estimate.

The end of thrusting is marked by the intrusion of post-collisional magmatic bodies into the hinterland (Chemale et al., 2012; Florisbal, Bitencourt, et al., 2012), and the partitioning and localization of strain into the Major Gercino Shear Zone (De Toni, Bitencourt, Konopásek, et al., 2020; Hueck, Basei, et al., 2018). Early syn-tectonic magmatism of the Florianópolis Batholith within the Major Gercino Shear Zone records a transition from flat-lying to upright transcurrent emplacement structures from ca. 625 to 615 Ma, and by ca. 610 Ma the syn-tectonic magmatic intrusions appear to be controlled entirely by sub-vertical transcurrent shear zones (Florisbal,

Bitencourt, et al., 2012). Thus, the period between ca. 635–615 Ma has been interpreted as the timing of progressive reorientation of the stress field resulting in the end of thrust-dominated tectonics, and the establishment of the simple shear-dominated Major Gercino Shear Zone and pure shear-dominated deformation in the foreland (De Toni, Bitencourt, Konopásek, et al., 2020). The majority of magmatism in the foreland was delayed by ca. 10 Myr with respect to the Florianópolis Batholith, starting from ca. 615 Ma (Campos et al., 2012; Florisbal, Janasi, Bitencourt, & Heaman, 2012; Hueck et al., 2019), and as the foreland granites crosscut the S_1 foliation the absolute minimum age for the end of thrusting-controlled exhumation in the foreland is constrained to ca. 615 Ma.

4.2.3. Pure Shear-Dominated Deformation, Granite Intrusion, and Retrograde Metamorphism (Ca. 615 to 550 Ma)

The shift to pure shear contractional deformation in the Brusque Complex is reflected by upright to steeply inclined F_2 folding, and the development of extensive sub-vertical S_2 cleavages and transposition foliations. As previously described, the S_2 structures are associated with retrograde chlorite overgrowth, which is particularly clear in the medium-grade domain (Figure 4b). Similarly, the S_2 transposition foliations and mylonites in the southern low-grade domain close to the Major Gercino Shear Zone are dominated by chlorite and muscovite, and relict garnet at some outcrops suggest that the apparent low-grade metamorphic conditions may be the result of intense retrograde overprint. However, garnet-bearing outcrops (e.g., locality BA23) are rare, and the reorientation and transposition of previous fabrics make it difficult to identify earlier structures and mineral assemblages. Thus, the S_2 structures are clearly shown to be retrogressive only in the garnet-bearing schists.

The upper limit for the timing of this deformation in the foreland is constrained by the S_1 biotite Ar–Ar cooling age at ca. 635 Ma. However, the lower-greenschist facies conditions recorded during S_2 development indicate higher temperatures than suggested by this cooling age. This can be explained by increasing thermal input from below by deep-seated melting after the end of thrusting, which is supported by exhumation of the Camboriú Complex and subsequent contact metamorphism of the overlying Brusque Complex (De Toni, Bitencourt, Konopásek, et al., 2020). Furthermore, the foreland granitic bodies, in particular the Valsungana Batholith, are preferentially elongated NE–SW with the main S_2 structural trend (Figure 2c) and show syn-kinematic magmatic foliation fabrics (Hueck et al., 2016) and overprinting metamorphic contact aureoles (Basei et al., 2011) suggesting that they intruded during or after the actively developing F_2 and S_2 structures. Thus, the development of F_2 and S_2 deformation structures likely started at or before ca. 615 Ma and continued throughout the period of granite intrusion.

Phase equilibria modeling and Lu–Hf dating of sample BA22 show that from at least ca. 600 Ma the Brusque Complex was located at a depth corresponding to ~2–3 kbar. However, *P–T* modeling of this sample estimates temperatures of over 500°C (Figure 7c), resulting in a high apparent thermal gradient of up to ~50°C/km (Figure 12b). Due to its proximity with the Valsungana and Florianópolis batholiths (Figure 1c), the high-T/low-P conditions experienced by this sample likely reflect high thermal input from adjacent magmatic rocks intruding the hinterland and/or foreland. Based on the preserved ca. 635 Ma cooling age from sample BC43, and the absence of garnet-bearing rocks in the majority of the complex, it is clear that there were large differences in local thermal conditions during the post-collisional period. These differences were likely controlled by proximity to magmatic intrusions, which in many cases have well developed metamorphic contact aureoles (Basei et al., 2011; Campos et al., 2012).

The muscovite Ar–Ar ages indicate that the Brusque Complex was still actively deforming from ca. 600 to 570 Ma. Although most deformation overprinting S_1 is pure shear-dominated F_2 folding and S_2 crenulation cleavage development, high-strain zones within the complex also show phyllonitic S_2 foliation fabrics with horizontal stretching lineations indicative of strike-slip deformation, suggesting that partitioning of the strike-slip component of transpression was not solely confined to the Major Gercino Shear Zone. This lasted until at least ca. 570 Ma (muscovite Ar–Ar sample BC30), which is ca. 15 Myr after the end of granitic magmatism (Chemale et al., 2012; Hueck et al., 2019). Localized ductile deformation in the Itajaí–Perimbó Shear Zone along the northern edge of the Schist Belt, at ca. 545 Ma, seemingly marks the end of contractional/transpressional deformation and coincides with late-stage deformation along the Major Gercino Shear Zone between ca. 580–540 Ma (Hueck, Basei, et al., 2018). Such timing supports interpretations that ca. 560 Ma orogenic foreland basin sediments were interleaved with the Brusque Complex during the later stages of orogenic development (Percival, Konopásek, Eiesland, et al., 2021).

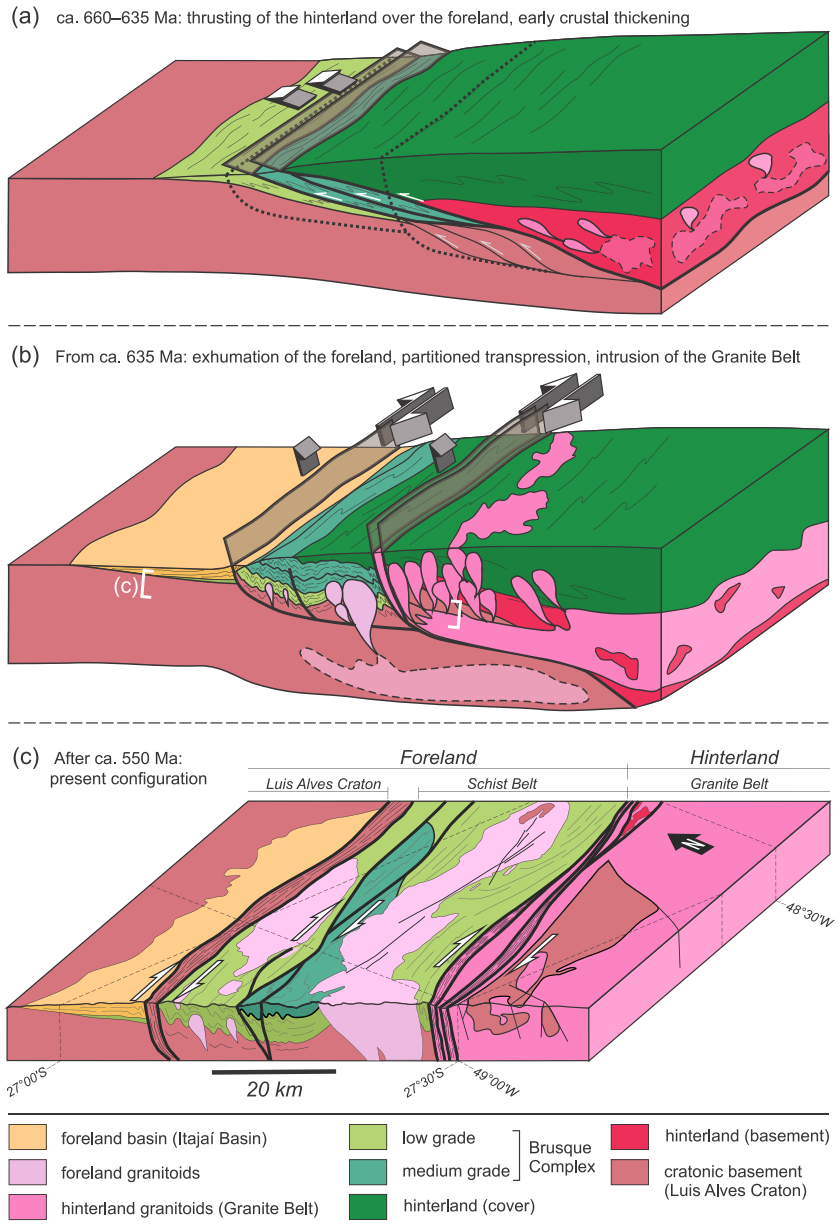

Figure 13. Schematic diagram outlining the proposed tectonic evolution of the northern Dom Feliciano Belt. (a) Between ca. 660–635 Ma: early crustal thickening and thrusting of the hinterland over Tonian volcanosedimentary supracrustal rocks (Brusque Complex) and the Luis Alves Craton (stippled lines show future shear zones, stippled polygons show early migmatization). (b) From ca. 635 Ma: partitioned transpression resulting in simple shear-dominated strike-slip deformation in the hinterland and pure shear-dominated deformation in the foreland; intrusion of the Granite Belt (from ca. 625 Ma) and foreland granites (from ca. 615 Ma). White frame shows location of cross section in Figure 13c. (c) From ca. 550 Ma: final configuration of the northern Dom Feliciano Belt.

4.3. Summary of the Two-Stage Tectonic Evolution of the Dom Feliciano Belt

The structural, metamorphic, and geochronological data presented in this study reveal two distinct stages for the tectonic evolution of the northern Dom Feliciano Belt: (a) early crustal thickening driven by top-to-NW thrusting and (b) partitioned transpression leading to upright folding of the foreland and strike-slip shearing at the contact between the hinterland and the foreland. As such, the data mostly support the evolutionary model proposed by De Toni, Bitencourt, Konopásek, et al. (2020) for the north-easternmost part of the Dom Feliciano Belt. Our proposed tectonic model is summarized in Figure 13.

Early orogenic thickening recorded in the northern Dom Feliciano Belt foreland at ca. 660–650 Ma was likely induced by thrusting of the hinterland over pre-orogenic rift sediments deposited on the Luis Alves cratonic basement (Figure 13a). Internal thrust planes developed within the Brusque Complex, and progressive thrusting toward the foreland led to the juxtaposition of the deeper-seated medium-grade domain over the low-grade domain, and the development of an inverted metamorphic gradient within the Brusque Complex (Figure 13a). Thickening of the foreland took place at progressively increasing apparent thermal gradients from ~25°C/km to ~35°C/km between ca. 660–650 Ma (Figure 12b). Thrusting-related exhumation in the foreland was likely finishing by ca. 635 Ma, at which time the foreland was sufficiently loaded by the thickened crust that it began to buckle and fold (Figure 13b), resulting in doming in the foreland and decompressive melting of the foreland basement.

The transition into partitioned transpression from ca. 635 Ma resulted in the development of predominantly upright folds and pure shear-dominated shear zones in the foreland, and dextral strike-slip shearing along its contact with the hinterland (Figure 13b). The thermal effect of crustal loading in the foreland became apparent at ca. 615 Ma when, with a delay of ca. 15–20 Myr compared to the hinterland, melting in the basement produced the foreland batholiths (Figure 13b). This is supported by metamorphic data from the supracrustal complex (this work) and the crystalline basement (De Toni, Bitencourt, Konopásek, et al., 2020), which show that high apparent thermal gradients of up to ~50°C/km developed in the period between ca. 635–600 Ma. The intrusion of magmatic rocks into the foreland was coeval with pure shear-dominated deformation, producing contact aureoles in the foreland metasedimentary rocks. From ca. 585 Ma, coinciding with the end of melting and final cooling of the orogen, low-temperature deformation in the Brusque Complex localized entirely into steep shear zones (Figures 13b and 13c).

4.4. Implications for the Pre-Orogenic Evolution of the Kaoko–Dom Feliciano–Gariep System

According to subduction-collision models involving the Adamastor Ocean, the Southern Brazilian Shear Belt (including the Major Gercino Shear Zone) represents the suture after ocean closure and thrusting of the magmatic arc—the Granite Belt— over the cratonic passive margin sediments—the Schist Belt (Basei et al., 2018, 2000; Hueck, Oyhantçabal, et al., 2018; Passarelli et al., 2010). This interpretation requires that orogenic crustal thickening in the western foreland post-dates intrusion of the Granite Belt, as continental collision could only occur after the closure of the Adamastor Ocean. However, our results show that crustal thickening in the foreland, between ca. 660–650 Ma, occurred ca. 20–30 Myr prior to the onset of large-scale melting and intrusion of the Granite Belt from ca. 630 Ma (Basei et al., 2021; Florisbal, Janasi, Bitencourt, & Heaman, 2012; Figures 13a and 13b). This gap in time corresponds well with observations and modeling from other orogens showing a ca. 20–25 Myr delay between crustal thickening and large-scale melting (England & Thompson, 1986; Jamieson & Beaumont, 2013; Jamieson et al., 2011). Thus, the timing of early orogenic thickening in the western foreland ca. 20–30 Myr prior to large-scale melting in the hinterland precludes the interpretation of the Granite Belt as a supra-subduction zone magmatic arc related to long-lived subduction of a large Adamastor Ocean.

Examples in the literature show that large-scale syn-orogenic melting is typical for hinterland domains in hot orogenic systems (e.g., Cavalcante et al., 2018; Jamieson et al., 2011; Vanderhaeghe, 2009; Vanderhaeghe & Teyssier, 2001). This is consistent with alternative interpretations of the Granite Belt as representing post-collisional magmatism driven by melting in the lower-to middle-crust with connections to the mantle (Bitencourt & Nardi, 2000; Florisbal, Bitencourt, et al., 2012; Florisbal et al., 2009; Florisbal, Janasi, Bitencourt, & Heaman, 2012; Florisbal, Janasi, Bitencourt, Nardi, et al., 2012).

These observations support recent interpretations of the pre-orogenic position of the Kaoko and Dom Feliciano belts within an intracontinental or back-arc rift setting, where the Luis Alves Craton and Nico Pérez Terrane represent parts of the rifted/attenuated margin of the Congo Craton. In such models, orogeny is the result of rift inversion triggered by the end of subduction and closure of an oceanic domain occurring farther to the west (in today's coordinates), documented by relict magmatic arcs in the São Gabriel Terrane at the western edge of the central Dom Feliciano Belt foreland (De Toni, Bitencourt, Nardi, et al., 2020; Konopásek et al., 2018, 2020; Oriolo, Oyhantçabal, Wemmer, Basei, et al., 2016). In the central part of the Dom Feliciano Belt, the potential arc-to-hinterland distance suggests a setting similar to accretionary orogeny (see De Toni, Bitencourt, Nardi, et al., 2020; Konopásek et al., 2018), while in its northern part the distance to a potential controlling subduction zone/arc system was probably large, which is more suggestive of an intracontinental setting (Konopásek et al., 2020).

The geochronological data presented in this study suggest that early crustal thickening in the Dom Feliciano Belt foreland coincides with, or slightly precedes, high temperature thrust-related metamorphism and early (but limited) magmatism in the hinterland between ca. 655–640 Ma (Chemale et al., 2012; Gross et al., 2009; Martil, 2016; Oyhantçabal et al., 2009; Will et al., 2019). Thus, crustal thickening in the hinterland and foreland was largely coeval. Crustal thickening on the South American side of the orogenic system coincides with early syn-orogenic sedimentation in the Kaoko Belt on the African side (Konopásek et al., 2017), implying proximity between the Congo and Luis Alves cratonic margins at ca. 660–650 Ma. Furthermore, the onset of crustal thickening on the western side of the orogen took place during, or shortly after, the end of crustal stretching recorded in the eastern (African) foreland between ca. 660–645 Ma (see discussion in Konopásek et al., 2020, 2017). These observations further preclude the presence of a large Adamastor Ocean between the African and South American crustal blocks at this time.

5. Conclusions

The Neoproterozoic orogenic evolution of the northern Dom Feliciano Belt is complex owing to a two-stage tectono-metamorphic history. Early convergence is recorded in the supracrustal rocks of the foreland (the Brusque Complex) by the development of a flat-lying metamorphic foliation (S_1) that formed during top-to-NW directed thrusting and records peak regional metamorphic conditions. Garnet-bearing schists record prograde metamorphism with peak *P–T* conditions estimated at 5.5–6.7 kbar and 540–570°C, indicating a geothermal gradient (~25°C/km) that is consistent with regional orogenic metamorphism during crustal thickening. Early garnet growth is constrained by garnet–whole rock Lu–Hf ages of 660 ± 2 Ma, 652 ± 2 Ma, and 649 ± 16 Ma, and the timing of peak regional metamorphism is constrained by a garnet–whole rock Sm–Nd age of 647 ± 10 Ma and a monazite U–Pb age of 641 ± 8 Ma. Exhumation of the foreland supracrustal rocks likely occurred between ca. 635–615 Ma, during which time deformation transitioned into a partitioned transpressional system with pure shear-dominated deformation localized in the foreland and dextral strike-slip deformation in the hinterland. This is marked by the development of upright, NE–SW trending orogen-parallel folds (F_2), a pervasive axial planar crenulation cleavage (S_2), and pure-to dextral strike-slip shear zones. By ca. 600 Ma, the complex was exhumed to pressures of 2.3–3.3 kbar (~10 km), and the intrusion of large granitic batholiths and metamorphic contact aureoles recording local apparent thermal gradients of up to ~50°C/km indicate increasing thermal input from below. Deformation within the foreland continued until at least ca. 570 Ma, and along major shear zones until ca. 545 Ma.

Our work shows that supracrustal sequences in the northern Dom Feliciano Belt foreland reached metamorphic conditions typical for crustal thickening between ca. 660–650 Ma. This is ca. 20–30 Myr prior to the onset of massive magmatic activity in the hinterland, which is a typical delay seen in hot internal parts of orogens during the collision. This observation contradicts a subduction-related magmatic arc interpretation of massive granitic magmatism in the Dom Feliciano Belt hinterland (the Granite Belt), and instead supports a post-collisional interpretation. This implies the absence of subduction at this time, and further suggests the absence of a large oceanic domain between the foreland and hinterland domains prior to orogenesis. Instead, we interpret orogenesis as being initiated by rift-basin inversion driven by far-field forces transmitted through the crust, potentially in an intracontinental setting or a back-arc rift setting with subduction and a true arc region located further to the west.

Acknowledgments
This work represents part of a PhD project which received financial support from Diku Norway and CAPES Brazil (project UTF-2018-10,004). J. Konopásek appreciates support from the Czech Science Foundation (project no. 18-24281S). This work was also partly supported by the Research Council of Norway through the funding to the Norwegian Research School on Dynamics and Evolution of Earth and Planets (DEEP), project number 249040/F60. Many thanks to D. Sala and M. Koziarska for their help with isotopic analytical work, and R. Škoda, R Čopjaková, and M. Erambert for providing monazite elemental maps and assistance with microprobe analyses. We thank M. Hueck and an anonymous reviewer for their helpful comments and suggestions.

Data Availability Statement

Whole-rock and mineral major element, garnet–whole-rock Lu–Hf and Sm–Nd geochronology, monazite U–Pb geochronology and trace element, and mica Ar–Ar geochronology data are available (Percival, Konopásek, Anczkiewicz, et al., 2021).

References

Aitken, A. R. A., Raimondo, T., & Capitanio, F. A. (2013). The intraplate character of supercontinent tectonics. *Gondwana Research*, *24*(3), 807–814. https://doi.org/10.1016/j.gr.2013.03.005

Anczkiewicz, R., Chakraborty, S., Dasgupta, S., Mukhopadhyay, D., & Kołtonik, K. (2014). Timing, duration and inversion of prograde Barrovian metamorphism constrained by high resolution Lu–Hf garnet dating: A case study from the Sikkim Himalaya, NE India. *Earth and Planetary Science Letters*, *407*, 70–81. https://doi.org/10.1016/j.epsl.2014.09.035

Anczkiewicz, R., Platt, J. P., Thirlwall, M. F., & Wakabayashi, J. (2004). Franciscan subduction off to a slow start: Evidence from high-precision Lu–Hf garnet ages on high grade-blocks. *Earth and Planetary Science Letters*, *225*(1), 147–161. https://doi.org/10.1016/j.epsl.2004.06.003

Anczkiewicz, R., Thirlwall, M., Alard, O., Rogers, N. W., & Clark, C. (2012). Diffusional homogenization of light REE in garnet from the Day Nui Con Voi Massif in N-Vietnam: Implications for Sm–Nd geochronology and timing of metamorphism in the red river shear zone. *Chemical Geology*, *318–319*, 16–30. https://doi.org/10.1016/j.chemgeo.2012.04.024

Anczkiewicz, R., & Thirlwall, M. F. (2003). Improving precision of Sm-Nd garnet dating by H2SO4 leaching: A simple solution to the phosphate inclusion problem. *Geological Society, London, Special Publications*, *220*(1), 83–91. https://doi.org/10.1144/GSL.SP.2003.220.01.05

Basei, M. A. S., Campos Neto, M. C., Castro, N. A., Nutman, A. P., Wemmer, K., Yamamoto, M. T., et al. (2011). Tectonic evolution of the Brusque group, dom feliciano belt, Santa Catarina, southern Brazil. *Journal of South American Earth Sciences*, *32*(4), 324–350. https://doi.org/10.1016/j.jsames.2011.03.016

Basei, M. A. S., Corrêa, V. X., Castro, N. A., & Hueck, M. (2021). U–Pb geochronology and Lu–Hf zircon isotopy of the Santinho granitic association: A remnant of the early magmatic stages of the Florianópolis batholith, Santa Catarina, Brazil. *Journal of South American Earth Sciences*, *108*, 103148. https://doi.org/10.1016/j.jsames.2020.103148

Basei, M. A. S., Frimmel, H. E., Campos Neto, M. d. C., de Araujo, C. E. G., de Castro, N. A., & Passarelli, C. R. (2018). The tectonic history of the southern Adamastor Ocean based on a correlation of the Kaoko and dom feliciano belts. In S. Siegesmund, M. A. S. Basei, P. Oyhantçabal, & S. Oriolo (Eds.), *Geology of Southwest Gondwana* (1st ed., p. 63–85). https://doi.org/10.1007/978-3-319-68920-3_3

Basei, M. A. S., Grasso, C. B., Vlach, S. R. F., Nutman, A., Siga, O., Jr, & Osaki, L. S. (2008). A-type rift-related granite and the lower cryogenian age for the beginning of the Brusque Belt basin. *Paper presented at the Proceedings of south American Symposium on isotope geology*. San Carlos de Bariloche.

Basei, M. A. S., Nutman, A., Siga, O., Jr, Passarelli, C. R., & Drukas, C. O. (2009). The evolution and tectonic setting of the Luis Alves Microplate of southeastern Brazil: An exotic terrane during the assembly of western Gondwana. In C. Gaucher, A. N. Sial, H. E. Frimmel, & G. P. Halverson (Eds.), *Developments in Precambrian geology* (Vol. 16, pp. 273–291). Elsevier.

Basei, M. A. S., Siga, O., Jr, Masquelin, H., Harara, O. M., Reis Neto, J. M., & Preciozzi, F. (2000). The dom feliciano belt of Brazil and Uruguay and its foreland domain, the Rio de la Plata craton: Framework, tectonic evolution and correlation with similar provinces of southwestern Africa. In U. G. Cordani, E. J. Milani, A. Thomaz Filho, & D. A. Campos (Eds.), *Tectonic evolution of south America* (p. 311–334). Geological Society.

Battisti, M. A., Bitencourt, M. F., De Toni, G. B., Nardi, L. V. S., & Konopásek, J. (2018). Metavolcanic rocks and orthogneisses from Porongos and Várzea do Capivarita complexes: A case for identification of tectonic interleaving at different crustal levels from structural and geochemical data in southernmost Brazil. *Journal of South American Earth Sciences*, *88*, 253–274. https://doi.org/10.1016/j.jsames.2018.08.009

Baxter, E. F., & Scherer, E. E. (2013). Garnet geochronology: Timekeeper of tectonometamorphic processes. *Elements*, *9*(6), 433–438. https://doi.org/10.2113/gselements.9.6.433

Bitencourt, M. F., & Nardi, L. V. S. (1993). Late- to post-collisional Brasiliano magmatism in southernmost Brazil. *Anais da Academia Brasileira de Ciências*, *65*, 3–16. https://doi.org/10.25249/0375-7536.2000301186189

Bitencourt, M. F., & Nardi, L. V. S. (2000). Tectonic setting and sources of magmatism related to the southern Brazilian shear belt. *Revista Brasileira de Geociencias*, *30*(1), 186–189.

Bosse, V., & Villa, I. M. (2019). Petrochronology and hygrochronology of tectono-metamorphic events. *Gondwana Research*, *71*, 76–90. https://doi.org/10.1016/j.gr.2018.12.014

Campos, R. S., Philipp, R. P., Massonne, H.-J., & Chemale, F., Jr. (2012). Early post-collisional Brasiliano magmatism in Botuverá region, Santa Catarina, southern Brazil: Evidence from petrology, geochemistry, isotope geology and geochronology of the diabase and lamprophyre dikes. *Journal of South American Earth Sciences*, *37*, 266–278. https://doi.org/10.1016/j.jsames.2012.02.005

Campos, R. S., Philipp, R. P., Massonne, H.-J., Chemale, F., Jr, & Theye, T. (2011). Petrology and isotope geology of mafic to ultramafic metavolcanic rocks of the Brusque Metamorphic Complex, southern Brazil. *International Geology Review*, *54*(6), 686–713. https://doi.org/10.1080/00206814.2011.569393

Cavalcante, C., Fossen, H., de Almeida, R. P., Hollanda, M. H. B. M., & Egydio-Silva, M. (2019). Reviewing the puzzling intracontinental termination of the Araçuaí-West Congo orogenic belt and its implications for orogenic development. *Precambrian Research*, *322*, 85–98. https://doi.org/10.1016/j.precamres.2018.12.025

Cavalcante, C., Hollanda, M. H., Vauchez, A., & Kawata, M. (2018). How long can the middle crust remain partially molten during orogeny? *Geology*, *46*(10), 839–842. https://doi.org/10.1130/g45126.1

Cawood, P. A., Kröner, A., Collins, W. J., Kusky, T. M., Mooney, W. D., & Windley, B. F. (2009). Accretionary orogens through Earth history. *Geological Society, London, Special Publications*, *318*(1), 1–36. https://doi.org/10.1144/SP318.1

Caxito, F. A., Heilbron, M., Valeriano, C. M., Bruno, H., Pedrosa-Soares, A., Alkmim, F. F., et al. (2021). Integration of elemental and isotope data supports a Neoproterozoic Adamastor Ocean realm. *Geochemical Perspectives Letters*, *17*, 6–10. https://doi.org/10.7185/geochemlet.2106

Chemale, F., Mallmann, G., Bitencourt, M. F., & Kawashita, K. (2012). Time constraints on magmatism along the major Gercino shear zone, southern Brazil: Implications for west Gondwana reconstruction. *Gondwana Research*, *22*(1), 184–199. https://doi.org/10.1016/j.gr.2011.08.018

Chemale, F., Philipp, R. P., Dussin, I. A., Formoso, M. L. L., Kawashita, K., & Berttotti, A. L. (2011). Lu–Hf and U–Pb age determination of Capivarita Anorthosite in the dom feliciano belt, Brazil. *Precambrian Research*, *186*(1–4), 117–126. https://doi.org/10.1016/j.precamres.2011.01.005

Cheng, H. (2019). Garnet Lu–Hf and Sm–Nd geochronology: A time capsule of the metamorphic evolution of orogenic belts. *Geological Society, London, Special Publications*, *474*(1), 47–67. https://doi.org/10.1144/sp474.7

Collins, W. J. (2002). Nature of extensional accretionary orogens. *Tectonics*, *21*(4), 6–12. https://doi.org/10.1029/2000TC001272

Connolly, J. A. D. (2005). Computation of phase equilibria by linear programming: A tool for geodynamic modeling and its application to subduction zone decarbonation. *Earth and Planetary Science Letters*, *236*(1–2), 524–541. https://doi.org/10.1016/j.epsl.2005.04.033

Cunningham, D. (2005). Active intracontinental transpressional mountain building in the Mongolian Altai: Defining a new class of orogen. *Earth and Planetary Science Letters*, *240*(2), 436–444. https://doi.org/10.1016/j.epsl.2005.09.013

De Toni, G. B., Bitencourt, M. F., Konopásek, J., Battisti, M. A., Oliveira da Costa, E., & Savian, J. F. (2021). Autochtonous origin of the Encruzilhada Block, Dom Feliciano Belt, southern Brazil, based on aerogeophysics, image analysis and PT-paths. *Journal of Geodynamics*, *144*, 101825. https://doi.org/10.1016/j.jog.2021.101825

De Toni, G. B., Bitencourt, M. F., Konopásek, J., Martini, A., Andrade, P. H. S., Florisbal, L. M., & Campos, R. S. (2020). Transpressive strain partitioning between the major Gercino shear zone and the Tijucas fold belt, dom feliciano belt, Santa Catarina, southern Brazil. *Journal of Structural Geology*, *136*, 104058. https://doi.org/10.1016/j.jsg.2020.104058

De Toni, G. B., Bitencourt, M. F., Nardi, L. V. S., Florisbal, L. M., Almeida, B. S., & Geraldes, M. (2020). Dom Feliciano Belt orogenic cycle tracked by its pre-collisional magmatism: The Tonian (ca. 800 Ma) Porto Belo Complex and its correlations in southern Brazil and Uruguay. *Precambrian Research*, *342*, 105702. https://doi.org/10.1016/j.precamres.2020.105702

England, P. C., & Thompson, A. (1986). Some thermal and tectonic models for crustal melting in continental collision zones. *Geological Society, London, Special Publications*, *19*(1), 83. https://doi.org/10.1144/GSL.SP.1986.019.01.05

Evans, T. P. (2004). A method for calculating effective bulk composition modification due to crystal fractionation in garnet-bearing schist: Implications for isopleth thermobarometry. *Journal of Metamorphic Geology*, *22*(6), 547–557. https://doi.org/10.1111/j.1525-1314.2004.00532.x

Faure, M., Shu, L., Wang, B., Charvet, J., Choulet, F., & Monie, P. (2009). Intracontinental subduction: A possible mechanism for the early Palaeozoic orogen of SE China. *Terra Nova*, *21*(5), 360–368. https://doi.org/10.1111/j.1365-3121.2009.00888.x

Fischer, G., Fassbinder, E., Barros, C. E. M., & Fossen, H. (2019). The evolution of quartz veins during the tectonometamorphic development of the Brusque Metamorphic Complex, Brazil. *Journal of South American Earth Sciences*, *93*, 174–182. https://doi.org/10.1016/j.jsames.2019.04.027

Florisbal, L. M., Bitencourt, M. F., Janasi, V. A., Nardi, L. V. S., & Heaman, L. M. (2012). Petrogenesis of syntectonic granites emplaced at the transition from thrusting to transcurrent tectonics in post-collisional setting: Whole-rock and Sr–Nd–Pb isotope geochemistry in the Neoproterozoic Quatro Ilhas and Mariscal Granites, Southern Brazil. *Lithos*, *153*, 53–71. https://doi.org/10.1016/j.lithos.2012.04.031

Florisbal, L. M., Bitencourt, M. F., Nardi, L. V. S., & Conceição, R. V. (2009). Early post-collisional granitic and coeval mafic magmatism of medium- to high-K tholeiitic affinity within the Neoproterozoic Southern Brazilian Shear Belt. *Precambrian Research*, *175*(1–4), 135–148. https://doi.org/10.1016/j.precamres.2009.09.003

Florisbal, L. M., Janasi, V. A., Bitencourt, M. F., & Heaman, L. M. (2012). Space–time relation of post-collisional granitic magmatism in Santa Catarina, southern Brazil: U–Pb LA-MC-ICP-MS zircon geochronology of coeval mafic–felsic magmatism related to the major Gercino shear zone. *Precambrian Research*, *216–219*, 132–151. https://doi.org/10.1016/j.precamres.2012.06.015

Florisbal, L. M., Janasi, V. A., Bitencourt, M. F., Nardi, L. V. S., & Heaman, L. M. (2012). Contrasted crustal sources as defined by whole-rock and Sr–Nd–Pb isotope geochemistry of neoproterozoic early post-collisional granitic magmatism within the Southern Brazilian Shear Belt, Camboriú, Brazil. *Journal of South American Earth Sciences*, *39*, 24–43. https://doi.org/10.1016/j.jsames.2012.06.013

Fossen, H., Cavalcante, C., Konopásek, J., Tieppo Meira, V., Almeida, R., Hollanda, M., & Trompette, R. (2020). A critical discussion of the subduction-collision model for the Neoproterozoic Araçuaí-West Congo orogen. *Precambrian Research*, *125*, 105715. https://doi.org/10.1016/j.precamres.2020.105715

Fossen, H., Cavalcante, G. C., & Almeida, R. P. d. (2017). Hot versus cold orogenic behavior: Comparing the Araçuaí-west Congo and the Caledonian orogens. *Tectonics*, *36*(10), 2159–2178. https://doi.org/10.1002/2017tc004743

Fossen, H., & Cavalcante, G. C. G. (2017). Shear zones—A review. *Earth-Science Reviews*, *171*, 434–455. https://doi.org/10.1016/j.earscirev.2017.05.002

Fossen, H., Cavalcante, G. C. G., Pinheiro, R. V. L., & Archanjo, C. J. (2019). Deformation – progressive or multiphase? *Journal of Structural Geology*, *125*, 82–99. https://doi.org/10.1016/j.jsg.2018.05.006

Frimmel, H. E., Basei, M. A. S., & Gaucher, C. (2011). Neoproterozoic geodynamic evolution of SW-Gondwana: A southern African perspective. *International Journal of Earth Sciences*, *100*, 323–354. https://doi.org/10.1007/s00531-010-0571-9

Fuhrman, M. L., & Lindsley, D. H. (1988). Ternary-feldspar modeling and thermometry. *American Mineralogist*, *73*(3–4), 201–215.

Godet, A., Guilmette, C., Labrousse, L., Smit, M. A., Cutts, J. A., Davis, D. W., & Vanier, M.-A. (2021). Lu–Hf garnet dating and the timing of collisions: Palaeoproterozoic accretionary tectonics revealed in the Southeastern Churchill Province, Trans-Hudson Orogen, Canada. *Journal of Metamorphic Geology*, 1–31. https://doi.org/10.1111/jmg.12599

Gross, A. O. M. S., Droop, G. T. R., Porcher, C. C., & Fernandes, L. A. D. (2009). Petrology and thermobarometry of mafic granulites and migmatites from the Chafalote Metamorphic Suite: New insights into the Neoproterozoic P–T evolution of the Uruguayan—Sul-Rio-Grandense shield. *Precambrian Research*, *170*(3–4), 157–174. https://doi.org/10.1016/j.precamres.2009.01.011

Grove, M., & Harrison, T. M. (1996). 40Ar* diffusion in Fe-rich biotite. *American Mineralogist*, *81*(7–8), 940–951. https://doi.org/10.2138/am-1996-7-816

Guadagnin, F., Chemale, F., Jr, Dussin, I. A., Jelinek, A. R., dos Santos, M. N., Borba, M. L., et al. (2010). Depositional age and provenance of the Itajaí Basin, Santa Catarina state, Brazil: Implications for SW Gondwana correlation. *Precambrian Research*, *180*(3–4), 156–182. https://doi.org/10.1016/j.precamres.2010.04.002

Hagen-Peter, G., Cottle, J. M., Smit, M., & Cooper, A. F. (2016). Coupled garnet Lu-Hf and monazite U-Pb geochronology constrain early convergent margin dynamics in the Ross orogen, Antarctica.(Report). *Journal of Metamorphic Geology*, *34*(4), 293–319. https://doi.org/10.1111/jmg.12182

Hand, M., & Sandiford, M. (1999). Intraplate deformation in central Australia, the link between subsidence and fault reactivation. *Tectonophysics*, *305*(1), 121–140. https://doi.org/10.1016/S0040-1951(99)00009-8

Harrison, T. M., Célérier, J., Aikman, A. B., Hermann, J., & Heizler, M. T. (2009). Diffusion of 40Ar in muscovite. *Geochimica et Cosmochimica Acta*, *73*(4), 1039–1051. https://doi.org/10.1016/j.gca.2008.09.038

Hartnady, C., Joubert, P., & Stowe, C. (1985). Proterozoic crustal evolution in southwestern Africa. *International Union of Geological Sciences*, *8*(4), 236–244. https://doi.org/10.18814/epiiugs/1985/v8i4/003

Heilbron, M., de Morisson Valeriano, C., Peixoto, C., Tupinambá, M., Neubauer, F., Dussin, I., et al. (2020). Neoproterozoic magmatic arc systems of the central Ribeira belt, SE-Brazil, in the context of the west-Gondwana pre-collisional history: A review. *Journal of South American Earth Sciences*, *103*, 102710. https://doi.org/10.1016/j.jsames.2020.102710

Heilbron, M., & Machado, N. (2003). Timing of terrane accretion in the Neoproterozoic–Eopaleozoic Ribeira orogen (se Brazil). *Precambrian Research*, *125*(1), 87–112. https://doi.org/10.1016/S0301-9268(03)00082-2

Heine, C., Zoethout, J., & Müller, R. D. (2013). Kinematics of the south Atlantic rift. *Solid Earth*, *4*(2), 215–253. https://doi.org/10.5194/se-4-215-2013

Hermann, J., & Rubatto, D. (2003). Relating zircon and monazite domains to garnet growth zones: Age and duration of granulite facies metamorphism in the val Malenco lower crust. *Journal of Metamorphic Geology*, *21*(9), 833–852. https://doi.org/10.1046/j.1525-1314.2003.00484.x

Höfig, D. F., Marques, J. C., Basei, M. A. S., Giusti, R. O., Kohlrausch, C., & Frantz, J. C. (2018). Detrital zircon geochronology (U-Pb LA-ICP-MS) of syn-orogenic basins in SW Gondwana: New insights into the cryogenian-Ediacaran of Porongos complex, dom feliciano belt, southern Brazil. *Precambrian Research*, *306*, 189–208. https://doi.org/10.1016/j.precamres.2017.12.031

Holland, T. J. B., & Powell, R. (2011). An improved and extended internally consistent thermodynamic dataset for phases of petrological interest, involving a new equation of state for solids. *Journal of Metamorphic Geology*, *29*(3), 333–383. https://doi.org/10.1111/j.1525-1314.2010.00923.x

Hollister, L. S. (1966). Garnet zoning: An interpretation based on the Rayleigh fractionation model. *Science*, *154*(3757), 1647–1651.

Hueck, M., Basei, M. A. S., & Castro, N. A. d. (2016). Origin and evolution of the granitic intrusions in the Brusque Group of the Dom Feliciano Belt, south Brazil: Petrostructural analysis and whole-rock/isotope geochemistry. *Journal of South American Earth Sciences*, *69*, 131–151. https://doi.org/10.1016/j.jsames.2016.04.004

Hueck, M., Basei, M. A. S., & Castro, N. A. d. (2019). Tracking the sources and the evolution of the late neoproterozoic granitic intrusions in the Brusque group, dom feliciano belt, south Brazil: LA-ICP-MS and SHRIMP geochronology coupled to Hf isotopic analysis. *Precambrian Research*, *338*, 105566. https://doi.org/10.1016/j.precamres.2019.105566

Hueck, M., Basei, M. A. S., Wemmer, K., Oriolo, S., Heidelbach, F., & Siegesmund, S. (2018). Evolution of the major Gercino shear zone in the dom feliciano belt, south Brazil, and implications for the assembly of southwestern Gondwana. *International Journal of Earth Sciences*, *108*(2), 403–425. https://doi.org/10.1007/s00531-018-1660-4

Hueck, M., Oyhantçabal, P., Basei, M., & Siegesmund, S. (2018). The dom feliciano belt in southern Brazil and Uruquay. In S. Siegesmund, M. A. S. Basei, P. Oyhantçabal, S. Oriolo, R. Oberhänsli, M. J. d. Wit, et al. (Eds.), *Geology of Southwest Gondwana* (1st ed., pp. 267–302). https://doi.org/10.1007/978-3-319-68920-3_11

Jamieson, R. A., & Beaumont, C. (2013). On the origin of orogens. *The Geological Society of America Bulletin*, *125*(11–12), 1671–1702. https://doi.org/10.1130/b30855.1

Jamieson, R. A., Unsworth, M. J., Harris, N. B. W., Rosenberg, C. L., & Schulmann, K. (2011). Crustal melting and the flow of Mountains. *Elements*, *7*(4), 253–260. https://doi.org/10.2113/gselements.7.4.253

Jochum, K. P., Weis, U., Schwager, B., Stoll, B., Wilson, S. A., Haug, G. H., et al. (2016). Reference values following ISO Guidelines for Frequently Requested rock reference materials. *Geostandards and Geoanalytical Research*, *40*(3), 333–350. https://doi.org/10.1111/j.1751-908X.2015.00392.x

Jochum, K. P., Weis, U., Stoll, B., Kuzmin, D., Yang, Q., Raczek, I., et al. (2011). Determination of reference values for NIST SRM 610–617 Glasses following ISO Guidelines. *Geostandards and Geoanalytical Research*, *35*(4), 397–429. https://doi.org/10.1111/j.1751-908X.2011.00120.x

Koester, E., Porcher, C. C., Pimentel, M. M., Fernandes, L. A. D., Vignol-Lelarge, M. L., Oliveira, L. D., & Ramos, R. C. (2016). Further evidence of 777 Ma subduction-related continental arc magmatism in Eastern Dom Feliciano Belt, southern Brazil: The Chácara das Pedras Orthogneiss. *Journal of South American Earth Sciences*, *68*, 155–166. https://doi.org/10.1016/j.jsames.2015.12.006

Konopásek, J., Cavalcante, C., Fossen, H., & Janoušek, V. (2020). Adamastor – An ocean that never existed? *Earth-Science Reviews*, *205*, 103201. https://doi.org/10.1016/j.earscirev.2020.103201

Konopásek, J., Hoffmann, K.-H., Sláma, J., & Košler, J. (2017). The onset of flysch sedimentation in the Kaoko belt (NW Namibia)—Implications for the pre-collisional evolution of the Kaoko–dom feliciano–Gariep orogen. *Precambrian Research*, *298*, 220–234. https://doi.org/10.1016/j.precamres.2017.06.017

Konopásek, J., Janoušek, V., Oyhantçabal, P., Sláma, J., & Ulrich, S. (2018). Did the circum-Rodinia subduction trigger the Neoproterozoic rifting along the Congo–Kalahari Craton margin? *International Journal of Earth Sciences*, *107*(5), 1859–1894. https://doi.org/10.1007/s00531-017-1576-4

Konopásek, J., Sláma, J., & Košler, J. (2016). Linking the basement geology along the Africa-south America coasts in the south Atlantic. *Precambrian Research*, *280*, 221–230. https://doi.org/10.1016/j.precamres.2016.05.011

Lapen, T. J., Johnson, C. M., Baumgartner, L. P., Mahlen, N. J., Beard, B. L., & Amato, J. M. (2003). Burial rates during prograde metamorphism of an ultra-high-pressure terrane: An example from Lago di Cignana, western Alps, Italy. *Earth and Planetary Science Letters*, *215*(1), 57–72. https://doi.org/10.1016/S0012-821X(03)00455-2

Lara, P., Oyhantçabal, P., & Belousova, E. (2020). Two distinct crustal sources for late neoproterozoic granitic magmatism across the Sierra Ballena shear zone, dom feliciano belt, Uruguay: Whole-rock geochemistry, zircon geochronology and Sr-Nd-Hf isotope evidence. *Precambrian Research*, *341*, 105625. https://doi.org/10.1016/j.precamres.2020.105625

Leech, M. L., Singh, S., Jain, A. K., Klemperer, S. L., & Manickavasagam, R. M. (2005). The onset of India–Asia continental collision: Early, steep subduction required by the timing of UHP metamorphism in the western Himalaya. *Earth and Planetary Science Letters*, *234*(1), 83–97. https://doi.org/10.1016/j.epsl.2005.02.038

Lenz, C., Fernandes, L. A. D., McNaughton, N. J., Porcher, C. C., & Masquelin, H. (2011). U–Pb SHRIMP ages for the Cerro Bori orthogneisses, dom feliciano belt in Uruguay: Evidences of a ∼800Ma magmatic and ∼650Ma metamorphic event. *Precambrian Research*, *185*(3), 149–163. https://doi.org/10.1016/j.precamres.2011.01.007

Lister, G., & Forster, M. (2009). Tectonic mode switches and the nature of orogenesis. *Lithos*, *113*(1), 274–291. https://doi.org/10.1016/j.lithos.2008.10.024

Lugmair, G. W., & Marti, K. (1978). Lunar initial 143Nd/144Nd: Differential evolution of the lunar crust and mantle. *Earth and Planetary Science Letters*, *39*(3), 349–357. https://doi.org/10.1016/0012-821X(78)90021-3

Martil, M. M. D. (2016). *O Magmatismo de Arco continental Pré-colisional (790 Ma) E a Reconstituição Espaço-temporal do Regime Transpressivo (650 Ma) No Complexo Várzea do Capivarita*. Retrieved from https://www.lume.ufrgs.br/handle/10183/149194

Martil, M. M. D., Bitencourt, M. F., Nardi, L. V. S., Koester, E., & Pimentel, M. M. (2017). Pre-collisional, Tonian (ca. 790 Ma) continental arc magmatism in southern Mantiqueira Province, Brazil: Geochemical and isotopic constraints from the Várzea do Capivarita Complex. *Lithos*, *274–275*, 39–52. https://doi.org/10.1016/j.lithos.2016.11.011

McCourt, S., Armstrong, R., Jelsma, H., & Mapeo, R. (2013). New U-Pb SHRIMP ages from the Lubango region, SW Angola: Insights into the Palaeoproterozoic evolution of the Angolan shield, southern Congo craton, Africa. *Geological Society London Special Publications*, *170*(2), 353–363. https://doi.org/10.1144/jgs2012-059

McDonough, W. F., & Sun, S.-s. (1995). The composition of the Earth. *Chemical Geology*, *120*(3), 223–253. https://doi.org/10.1016/0009-2541(94)00140-4

Meira, V. T., Garcia-Casco, A., Hyppolito, T., Juliani, C., & Schorscher, J. H. D. (2019). Tectono-metamorphic evolution of the central Ribeira belt, Brazil: A case of late neoproterozoic intracontinental orogeny and flow of partially molten deep crust during the assembly of West Gondwana. *Tectonics*, *38*(8), 3182–3209. https://doi.org/10.1029/2018tc004959

Oliveira, C. H. E., Chemale, F., Jelinek, A. R., Bicca, M. M., & Philipp, R. P. (2014). U–Pb and Lu–Hf isotopes applied to the evolution of the late to post-orogenic transtensional basins of the dom feliciano belt, Brazil. *Precambrian Research*, *246*, 240–255. https://doi.org/10.1016/j.precamres.2014.03.008

Oriolo, S., Oyhantçabal, P., Basei, M. A. S., Wemmer, K., & Siegesmund, S. (2016). The Nico Pérez terrane (Uruguay): From Archean crustal growth and connections with the Congo craton to late neoproterozoic accretion to the Río de la Plata craton. *Precambrian Research*, *280*, 147–160. https://doi.org/10.1016/j.precamres.2016.04.014

Oriolo, S., Oyhantçabal, P., Wemmer, K., Basei, M. A. S., Benowitz, J., Pfänder, J., et al. (2016). Timing of deformation in the Sarandí del Yí Shear Zone, Uruguay: Implications for the amalgamation of western Gondwana during the Neoproterozoic Brasiliano-Pan-African Orogeny. *Tectonics*, *35*(3), 754–771. https://doi.org/10.1002/2015tc004052

Oriolo, S., Oyhantçabal, P., Wemmer, K., Heidelbach, F., Pfänder, J., Basei, M. A. S., et al. (2016). Shear zone evolution and timing of deformation in the Neoproterozoic transpressional Dom Feliciano Belt, Uruguay. *Journal of Structural Geology*, *92*, 59–78. https://doi.org/10.1016/j.jsg.2016.09.010

Oyhantçabal, P., Oriolo, S., Philipp, R. P., Wemmer, K., & Siegesmund, S. (2018). The Nico Pérez terrane of Uruguay and southeastern Brazil. In S. Siegesmund, M. A. S. Basei, P. Oyhantçabal, & S. Oriolo (Eds.), *Geology of Southwest Gondwana* (pp. 161–188). Springer International Publishing.

Oyhantçabal, P., Oriolo, S., Wemmer, K., Basei, M. A. S., Frei, D., & Siegesmund, S. (2021). Provenance of metasedimentary rocks of the western Dom Feliciano Belt in Uruguay: Insights from U–Pb detrital zircon geochronology, Hf and Nd model ages, and geochemical data. *Journal of South American Earth Sciences*, *108*, 103139. https://doi.org/10.1016/j.jsames.2020.103139

Oyhantçabal, P., Siegesmund, S., & Wemmer, K. (2011). The Río de la Plata craton: A review of units, boundaries, ages and isotopic signature. *International Journal of Earth Sciences*, *100*(2), 201–220. https://doi.org/10.1007/s00531-010-0580-8

Oyhantçabal, P., Siegesmund, S., Wemmer, K., Frei, R., & Layer, P. (2007). Post-collisional transition from calc-alkaline to alkaline magmatism during transcurrent deformation in the southernmost Dom Feliciano Belt (Braziliano–Pan-African, Uruguay). *Lithos*, *98*(1–4), 141–159. https://doi.org/10.1016/j.lithos.2007.03.001

Oyhantçabal, P., Siegesmund, S., Wemmer, K., & Passchier, C. W. (2011). The transpressional connection between dom feliciano and Kaoko belts at 580–550 Ma. *International Journal of Earth Sciences*, *100*, 379–390. https://doi.org/10.1007/s00531-010-0577-3

Oyhantçabal, P., Siegesmund, S., Wemmer, K., Presnyakov, S., & Layer, P. (2009). Geochronological constraints on the evolution of the southern dom feliciano belt (Uruguay). *Journal of the Geological Society*, *166*(6), 1075–1084. https://doi.org/10.1144/0016-76492008-122

Passarelli, C. R., Basei, M. A. S., Siga, O., Reath, I. M., & Campos Neto, M. d. C. (2010). Deformation and geochronology of syntectonic granitoids emplaced in the major Gercino shear zone, southeastern south America. *Gondwana Research*, *17*(4), 688–703. https://doi.org/10.1016/j.gr.2009.09.013

Pedrosa-Soares, A. C., Noce, C. M., Wiedemann, C. M., & Pinto, C. P. (2001). The Araçuaí-west-Congo orogen in Brazil: An overview of a confined orogen formed during Gondwanaland assembly. *Precambrian Research*, *110*(1), 307–323. https://doi.org/10.1016/S0301-9268(01)00174-7

Percival, J. J., Konopásek, J., Anczkiewicz, R., Ganerød, M., Sláma, J., Campos, R. S., & Bitencourt, M. F. (2021). Mineral geochemistry and geochronology from metamorphic rocks of the Brusque Complex, Dom Feliciano Belt, Brazil, Version 1.0. *Interdisciplinary Earth Data Alliance (IEDA)*. https://doi.org/10.26022/IEDA/112054

Percival, J. J., Konopásek, J., Eiesland, R., Sláma, J., de Campos, R. S., Battisti, M. A., & Bitencourt, M. d. F. (2021). Pre-orogenic connection of the foreland domains of the Kaoko–Dom Feliciano–Gariep orogenic system. *Precambrian Research*, *354*, 106060. https://doi.org/10.1016/j.precamres.2020.106060

Pertille, J., Hartmann, L. A., Santos, J. O. S., McNaughton, N. J., & Armstrong, R. (2017). Reconstructing the cryogenian–Ediacaran evolution of the Porongos fold and thrust belt, southern Brasiliano orogen, based on zircon U–Pb–Hf–O isotopes. *International Geology Review*, *59*(12), 1532–1560. https://doi.org/10.1080/00206814.2017.1285257

Peternell, M., Bitencourt, M. d. F., Kruhl, J. H., & Stäb, C. (2010). Macro and microstructures as indicators of the development of syntectonic granitoids and host rocks in the Camboriú region, Santa Catarina, Brazil. *Journal of South American Earth Sciences*, *29*(3), 738–750. https://doi.org/10.1016/j.jsames.2009.11.006

Philipp, R. P., & Machado, R. (2005). The late neoproterozoic granitoid magmatism of the Pelotas batholith, southern Brazil. *Journal of South American Earth Sciences*, *19*(4), 461–478. https://doi.org/10.1016/j.jsames.2005.06.010

Philipp, R. P., Mallmann, G., Bitencourt, M. F., Souza, E. R., Liz, J. D., Wild, F., et al. (2004). Caracterização Litológica e Evolução Metamórfica da Porção Leste do Complexo Metamórfico Brusque, Santa Catarina. *Revista Brasileira de Geociencias*, *34*, 21–34. https://doi.org/10.25249/0375-7536.20043412134

Philipp, R. P., Massonne, H.-J., & Campos, R. S. (2013). Peraluminous leucogranites of the Cordilheira suite: A record of neoproterozoic collision and the generation of the Pelotas batholith, dom feliciano belt, southern Brazil. *Journal of South American Earth Sciences*, *43*, 1532–1560. https://doi.org/10.1016/j.jsames.2012.10.006

Philipp, R. P., Pimentel, M. M., & Basei, M. A. S. (2018). The tectonic evolution of the São Gabriel terrane, dom feliciano belt, southern Brazil: The closure of the Charrua ocean. In S. Siegesmund, M. A. S. Basei, P. Oyhantçabal, & S. Oriolo (Eds.), *Geology of Southwest Gondwana* (pp. 243–265). https://doi.org/10.1007/978-3-319-68920-3_10

Pollington, A. D., & Baxter, E. F. (2010). High resolution Sm–Nd garnet geochronology reveals the uneven pace of tectonometamorphic processes. *Earth and Planetary Science Letters*, *293*(1), 63–71. https://doi.org/10.1016/j.epsl.2010.02.019

Porada, H. (1979). The Damara-Ribeira orogen of the Pan-African–Brasiliano cycle in Namibia (Southwest Africa) and Brazil as interpreted in terms of continental collision. *Tectonophysics*, *57*(2), 237–265. https://doi.org/10.1016/0040-1951(79)90150-1

Porada, H. (1989). Pan-African rifting and orogenesis in southern to equatorial Africa and eastern Brazil. *Precambrian Research*, *44*(2), 103–136. https://doi.org/10.1016/0301-9268(89)90078-8

Raimondo, T., Hand, M., & Collins, W. J. (2014). Compressional intracontinental orogens: Ancient and modern perspectives. *Earth-Science Reviews*, *130*, 128–153. https://doi.org/10.1016/j.earscirev.2013.11.009

Rubatto, D., Hermann, J., & Buick, I. S. (2006). Temperature and bulk composition control on the growth of monazite and zircon during low-pressure Anatexis (mount Stafford, Central Australia). *Journal of Petrology*, *47*(10), 1973–1996. https://doi.org/10.1093/petrology/egl033

Saalmann, K., Gerdes, A., Lahaye, Y., Hartmann, L., Remus, M., & Läufer, A. (2011). Multiple accretion at the eastern margin of the Rio de la Plata craton: The prolonged Brasiliano orogeny in southernmost Brazil. *International Journal of Earth Sciences*, *100*, 1532–1560. https://doi.org/10.1007/s00531-010-0564-8

Scherer, E. E., Cameron, K. L., & Blichert-Toft, J. (2000). Lu–Hf garnet geochronology: Closure temperature relative to the Sm–Nd system and the effects of trace mineral inclusions. *Geochimica et Cosmochimica Acta*, *64*(19), 3413–3432. https://doi.org/10.1016/S0016-7037(00)00440-3

Scherer, E. E., Munker, C., & Mezger, K. (2001). Calibration of the Lutetium-Hafnium clock. *Science*, *293*(5530), 683–687. https://doi.org/10.1126/science.1061372

Schmidt, A., Pourteau, A., Candan, O., & Oberhänsli, R. (2015). Lu–Hf geochronology on cm-sized garnets using microsampling: New constraints on garnet growth rates and duration of metamorphism during continental collision (Menderes Massif, Turkey). *Earth and Planetary Science Letters*, *432*, 24–35. https://doi.org/10.1016/j.epsl.2015.09.015

Silva, L. C., Hartmann, L. A., McNaughton, N. J., & Fletcher, I. (2000). Zircon U-Pb SHRIMP dating of a Neoproterozoic overprint in Paleoproterozoic granitic-gneissic terranes, southern Brazil. *American Mineralogist*, *85*(5–6), 649–667. https://doi.org/10.2138/am-2000-5-602

Smit, M. A., Hacker, B. R., & Lee, J. (2014). Tibetan garnet records early Eocene initiation of thickening in the Himalaya. *Geology*, *42*(7), 591–594. https://doi.org/10.1130/g35524.1

Stipp, M., Stünitz, H., Heilbronner, R., & Schmid, S. M. (2002). The eastern Tonale fault zone: A 'natural laboratory' for crystal plastic deformation of quartz over a temperature range from 250 to 700°C. *Journal of Structural Geology*, *24*(12), 1861–1884. https://doi.org/10.1016/S0191-8141(02)00035-4

Tedeschi, M., Novo, T., Pedrosa-Soares, A., Dussin, I., Tassinari, C., Silva, L. C., et al. (2016). The Ediacaran Rio Doce magmatic arc revisited (Araçuaí-Ribeira orogenic system, SE Brazil). *Journal of South American Earth Sciences*, *68*, 167–186. https://doi.org/10.1016/j.jsames.2015.11.011

Thompson, A. B., Schulmann, K., Jezek, J., & Tolar, V. (2001). Thermally softened continental extensional zones (arcs and rifts) as precursors to thickened orogenic belts. *Tectonophysics*, *332*(1–2), 115–141. https://doi.org/10.1016/S0040-1951(00)00252-3

Vance, D., & Keith O'Nions, R. (1992). Prograde and retrograde thermal histories from the central Swiss Alps. *Earth and Planetary Science Letters*, *114*(1), 113–129. https://doi.org/10.1016/0012-821X(92)90155-O

Vanderhaeghe, O. (2009). Migmatites, granites and orogeny: Flow modes of partially-molten rocks and magmas associated with melt/solid segregation in orogenic belts. *Tectonophysics*, *477*(3), 119–134. https://doi.org/10.1016/j.tecto.2009.06.021

Vanderhaeghe, O., & Teyssier, C. (2001). Partial melting and flow of orogens. *Tectonophysics*, *342*(3), 451–472. https://doi.org/10.1016/S0040-1951(01)00175-5

Vollmer, F. W. (1990). An application of eigenvalue methods to structural domain analysis. *The Geological Society of America Bulletin*, *102*(6), 786–791. https://doi.org/10.1130/0016-7606(1990)102<0786:AAOEMT>2.3.CO;2

Vollmer, F. W. (1995). C program for automatic contouring of spherical orientation data using a modified Kamb method. *Computers & Geosciences*, *21*(1), 31–49. https://doi.org/10.1016/0098-3004(94)00058-3

Warren, C. J., Greenwood, L. V., Argles, T. W., Roberts, N. M. W., Parrish, R. R., & Harris, N. B. W. (2018). Garnet-monazite rare earth element relationships in sub-solidus metapelites: A case study from Bhutan. *Geological Society Special Publication*, *478*(1), 145–166. https://doi.org/10.1144/SP478.1

White, R. W., Powell, R., & Clarke, G. L. (2002). The interpretation of reaction textures in Fe-rich metapelitic granulites of the Musgrave block, central Australia: Constraints from mineral equilibria calculations in the system K2O–FeO–MgO–Al2O3–SiO2–H2O–TiO2–Fe2O3. *Journal of Metamorphic Geology*, *20*(1), 41–55. https://doi.org/10.1046/j.0263-4929.2001.00349.x

White, R. W., Powell, R., Holland, T. J. B., Johnson, T. E., & Green, E. C. R. (2014). New mineral activity–composition relations for thermodynamic calculations in metapelitic systems. *Journal of Metamorphic Geology*, *32*(3), 261–286. https://doi.org/10.1111/jmg.12071

White, R. W., Powell, R., Holland, T. J. B., & Worley, B. A. (2000). The effect of TiO2 and Fe2O3 on metapelitic assemblages at greenschist and amphibolite facies conditions: Mineral equilibria calculations in the system K2O–FeO–MgO–Al2O3–SiO2–H2O–TiO2–Fe2O3. *Journal of Metamorphic Geology*, *18*(5), 497–511. https://doi.org/10.1046/j.1525-1314.2000.00269.x

Whitney, D., & Evans, B. (2010). Abbreviations for names of rock-forming minerals. *American Mineralogist*, *95*, 185–187. https://doi.org/10.2138/am.2010.3371

Will, T. M., Gaucher, C., Ling, X. X., Li, X. H., Li, Q. L., & Frimmel, H. E. (2019). Neoproterozoic magmatic and metamorphic events in the Cuchilla Dionisio terrane, Uruguay, and possible correlations across the south Atlantic. *Precambrian Research*, *320*, 303–322. https://doi.org/10.1016/j.precamres.2018.11.004

Winter, J. D. (2014). *Principles of igneous and metamorphic petrology* (2nd ed.). Pearson Education.

Zwart, H. J. (1962). On the determination of polymetamorphic mineral associations, and its application to the Bosost Area (Central Pyrenees). *International Journal of Earth Sciences*, *52*(1), 38–65. https://doi.org/10.1007/BF01840064

References From the Supporting Information

Budzyń, B., Sláma, J., Corfu, F., Crowley, J., Schmitz, M., Williams, M. L., et al. (2021). TS-Mnz—A new monazite age reference material for U-Th-Pb microanalysis. *Chemical Geology*, *572*, 120195.

Gonçalves, G. O., Lana, C., Scholz, R., Buick, I. S., Gerdes, A., Kamo, S. L., et al. (2016). An assessment of monazite from the Itambé pegmatite district for use as U–Pb isotope reference material for microanalysis and implications for the origin of the "Moacyr" monazite. *Chemical Geology*, *424*, 30–50.

Hartman, J., Franks, R., Gehrels, G., Hourigan, J., & Wenig, P. (2017). *Decoding dat files from a Thermo ElementTM ICP mass spectrometer*. Retrieved from https://github.com/jhh67/extractdat.git

Horstwood, M. S. A., Košler, J., Gehrels, G., Jackson, S. E., McLean, N. M., Paton, C., et al. (2016). Community-derived standards for LA-ICP-MS U-(Th-)Pb geochronology—Uncertainty Propagation, age interpretation and data reporting. *Geostandards and Geoanalytical Research*, *40*, 311–332.

Lee, J.-Y., Marti, K., Severinghaus, J. P., Kawamura, K., Yoo, H.-S., Lee, J. B., & Kim, J. S. (2006). A redetermination of the isotopic abundances of atmospheric Ar. *Geochimica et Cosmochimica Acta*, *70*(17), 4507–4512. https://doi.org/10.1016/j.gca.2006.06.1563

Ludwig, K. R. (2008). *User's Manual for Isoplot 3.70: A Geochronological Toolkit for Microsoft Excel* (Vol. 4, pp. 1–76). Berkeley Geochronological Center, Special Publication.

McDougall, I., & Harrison, T. M. (1999). *Geochronology and thermochronology by the 40Ar/39Ar method*. Oxford University Press.

Paton, C., Hellstrom, J., Paul, B., Woodhead, J., & Hergt, J. (2011). Iolite: Freeware for the visualisation and processing of mass spectrometric data. *Journal of Analytical Atomic Spectrometry*, *26*(12), 2508–2518. https://doi.org/10.1039/C1JA10172B

Petrus, J. A., & Kamber, B. S. (2012). VizualAge: A novel approach to laser ablation ICP-MS U-Pb geochronology data reduction. *Geostandards and Geoanalytical Research*, *36*, 247–270.

Renne, P. R., Mundil, R., Balco, G., Min, K., & Ludwig, K. R. (2010). Joint determination of 40K decay constants and 40Ar*/40K for the Fish Canyon sanidine standard, and improved accuracy for 40Ar/39Ar geochronology. *Geochimica et Cosmochimica Acta*, *74*(18), 5349–5367. https://doi.org/10.1016/j.gca.2010.06.017

Tunheng, A., & Hirata, T. (2004). Development of signal smoothing device for precise elemental analysis using laser ablation-ICP-mass spectrometry. *Journal of Analytical Atomic Spectrometry*, *19*(7), 932–934. https://doi.org/10.1039/B402493A

van Achterberg, E., Ryan, C., Jackson, S., & Griffin, W. (2001). Data reduction software for LA-ICP-MS. *Laser Ablation ICP-MS in the Earth Science*, *29*, 239–243.

Woodhead, J. D., Hellstrom, J., Hergt, J. M., Greig, A., & Maas, R. (2007). Isotopic and elemental imaging of geological materials by laser ablation inductively coupled plasma-mass spectrometry. *Geostandards and Geoanalytical Research*, *31*(4), 331–343. https://doi.org/10.1111/j.1751-908X.2007.00104.x